

**UNIVERSIDADE DO ESTADO DE SANTA CATARINA – UDESC
CENTRO DE CIÊNCIAS TECNOLÓGICAS – CCT
PÓS-GRADUAÇÃO EM CIÊNCIA E ENGENHARIA DE MATERIAIS – PGCEM**

André Koerich Ramos

Shrinkage Porosity Formation during Solidification in Compacted Graphite Iron

Master dissertation presented to the Master in Materials Science and Engineering program from the technical sciences center of the Santa Catarina State University, as a requirement to obtain the Master in Materials Science and Engineering degree.

Supervisor: Prof. Dr. Wilson Luiz Guesser

**JOINVILLE
2018**

Ramos, André Koerich
Shrinkage Porosity Formation during
Solidification in Compacted Graphite Iron / André
Koerich Ramos. -- 2018.
85 p.

Orientador: Wilson Luiz Guesser
Dissertação (Mestrado) -- Universidade do Estado de
Santa Catarina, Centro de Ciências Tecnológicas,
Programa de Pós-Graduação -- Selecionado --, 2018.

1. Cast Iron. 2. Solidification. 3. Compacted
Graphite Iron. 4. Shrinkage Porosity. I. Guesser,
Wilson Luiz. II. Universidade do Estado de Santa
Catarina. Programa de Pós-Graduação. III. Título.

Shrinkage Porosity Formation during Solidification in Compacted Graphite Iron

por

André Koerich Ramos

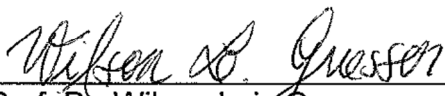
Esta dissertação foi julgada adequada para obtenção do título de

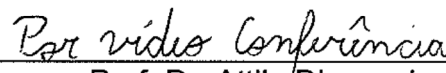
MESTRE EM CIÊNCIA E ENGENHARIA DE MATERIAIS

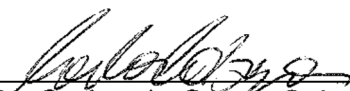
Área de concentração em "Metais"
e aprovada em sua forma final pelo

CURSO DE MESTRADO ACADÊMICO EM CIÊNCIA E ENGENHARIA DE
MATERIAIS DO CENTRO DE CIÊNCIAS TECNOLÓGICAS DA
UNIVERSIDADE DO ESTADO DE SANTA CATARINA.

Banca Examinadora:


Prof. Dr. Wilson Luiz Guesser
CCT/UEDESC (Orientador/Presidente)


Prof. Dr. Attila Dioszegi
Jönköping University


Dr. Carlos de Souza Cabezas
TUPY S.A

ABSTRACT

The present performance demands for diesel engines, in terms of thermal and mechanical loading, are requiring more and more developments of the materials used in components manufacturing. Compacted graphite iron (CGI) is presenting itself as a very good alternative material for use in the automotive industry. CGI higher mechanical strength, with thermal conductivity a little lower compared to lamellar graphite iron (LGI) and much higher compared to spheroidal graphite iron (SGI), makes it the perfect alternative for substitution of LGI in applications such as cylinder blocks and cylinder heads.

Compacted graphite iron presents approximately double of the fatigue limit of traditional grey iron and its higher mechanical properties also increases dimensional stability of the engines, which adds to a higher performance achievement. However, these advantages come with a cost, not only the material requires a narrower process window to produce it as it is more susceptible to casting defects such as shrinkage porosity, what demands studies to understand the mechanisms that leads to its formation.

This work studies the solidification of CGI, especially the effects of two important process parameters over the formation of microstructure and its relation to shrinkage porosity formation, magnesium content and degree of inoculation.

To study those variables a cast piece geometry is proposed, which is prone to shrinkage occurrence when varying at least one of the variables. Using this geometry, an experiment was designed using three different levels of both magnesium content and inoculation level, resulting in a three by three matrix for the experiment.

Techniques such as color etching and electron microprobe analysis are applied in order to analyze microstructural features of the material, such as eutectic cells structure and nodules distribution. Non-destructive testing is applied to evaluate shrinkage occurrence.

Keywords: Cast Iron, Solidification, Compacted Graphite Iron, Shrinkage Porosity.

RESUMO

A atual demanda por performance dos motores a diesel, em termos de requisitos mecânicos e térmicos, requer cada vez mais desenvolvimentos dos materiais utilizados para a fabricação dos componentes. O ferro fundido vermicular (FFV) tem se mostrado como uma boa alternativa para utilização na indústria automotiva. A maior resistência mecânica, com condutividade térmica um pouco inferior ao ferro fundido cinzento (FFC), mas muito superior à do ferro fundido nodular (FFN), faz com que o FFV seja a alternativa perfeita para a substituição do FFC em aplicações como blocos de motor e cabeçotes.

O FFV apresenta aproximadamente o dobro de resistência a fadiga do FFC e suas elevadas propriedades mecânicas também aumentam a estabilidade dimensional dos motores, o que o ajuda a atingir melhores performances. No entanto, essas vantagens vêm com um custo, o material não apenas exige uma janela de processo mais estreita para a sua produção, como ele apresenta maior susceptibilidade a ocorrência de defeitos de fundição, tais como rechupe, o que demanda estudos que aumentem o conhecimento dos mecanismos que levam a sua formação.

Este trabalho estuda a solidificação do FFV, especialmente os efeitos de duas importantes variáveis de processo sobre a formação da microestrutura e sua relação com a formação de rechupes, são eles o teor de magnésio e o grau de inoculação.

Para o estudo destas variáveis, um corpo de prova sensível a ocorrência de rechupe quando ocorre a variação de pelo menos uma das variáveis é proposto. Um experimento é desenvolvido utilizando este corpo de prova, utilizando três diferentes níveis de magnésio e grau de inoculação, resultando em uma matriz de resultados de três por três.

Técnicas como metalografia e ataque colorido são utilizadas para a análise microestrutural do material, tais como a estrutura de células eutéticas e a distribuição de nódulos. Técnicas não destrutivas são utilizadas para a avaliação da ocorrência de porosidades.

Palavras Chave: Ferro Fundido, Solidificação, Ferro Fundido Vermicular, Rechupe.

ACKNOWLEDGEMENTS

I would like to express my gratitude to:

My supervisor, Professor Wilson Luiz Guessser, for his support and incentive during all my work. For all his enthusiasm for the cast iron field for sharing this enthusiasm.

Professor Attila Diószegi, for his guidance during all my studies and for all his support and attention during my year at Jönköping.

All my colleagues at Tupy S.A. for their support during my work.

All the friends that I had the opportunity to meet at Jönköping.

Tupy S.A. staff for their assistance during the experiment development and execution.

UDESC and Jönköping University for their support during my studies.

Tupy S.A. for supporting and contributing to this work.

To my family, for their love and support all the time. Especially to my wife, Franciele, for her love and support and for always being by my side.

André Koerich Ramos
Joinville, September 2018

TABLE OF CONTENTS

1 INTRODUCTION.....	13
1.1 MAIN OBJECTIVE.....	14
1.2 SPECIFIC OBJECTIVES	14
2 LITERATURE REVIEW	15
2.1 CAST IRON.....	15
2.1.1 Compacted graphite iron (CGI) production	16
2.2 SOLIDIFICATION OF CAST IRON	21
2.2.1 Nucleation Process	22
2.2.2 Growth Process	22
2.2.3 Constitutional undercooling	24
2.2.4 The Coupled zone.....	25
2.2.5 Austenite Primary Phase Formation in Cast Irons	28
2.2.6 Eutectic Formation in Cast Irons.....	29
2.2.7 Double population of eutectic cells and nodules.....	33
2.2.8 Microsegregation.....	35
2.3 SHRINKAGE IN CAST IRON.....	37
2.3.1 Shrinkage porosity.....	39
3 EXPERIMENTAL PROCEDURE	45
3.1 SPECIMEN GEOMETRY AND EXPERIMENTAL ARRANGEMENT	45
3.2 MATERIALS	51
3.2.1 Nodularization treatment.....	53
3.3 CHEMICAL ANALYSIS	53
3.4 MICROSTRUCTURAL CHARACTERIZATION	54
3.4.1 Graphite Analysis.....	54
3.4.2 Color Etching	54
3.4.3 Eutectic Cell Analysis	55
4 RESULTS AND DISCUSSION	57
4.1 INFLUENCE OF THE STUDIED PARAMETERS OVER NODULARITY	57
4.2 COLOUR ETCHING INVESTIGATION	60
4.2.1 Region A	60
4.2.2 Region B.....	65
4.3 INFLUENCE OF THE STUDIED PARAMETERS OVER EUTECTIC CELL SIZE AND DISTRIBUTION.....	67
4.4 POROSITY	69
4.4.1 X-Ray Inspection.....	69
4.4.2 Ultrasonic Testing	71

4.4.3 Pore Surface Analysis with SEM and EDS	72
4.4.4 Porosity Formation Related to the Parameters under Study	74
5 CONCLUSIONS	77
6 FUTURE WORK	79
7 BIBLIOGRAPHIC REFERENCES	81

1 INTRODUCTION

The application of compacted graphite iron to engine components has increased during the last years due to the growing environment and fuel consumption requirements imposed by government agencies. [1] [2] A way of meeting these requirements is to generate an increase in both thermal and mechanical properties of the cylinder block and compacted graphite cast iron represents a viable solution to this challenge. [1]

The main reason for the higher mechanical properties of compacted graphite iron over lamellar graphite iron lies on its microstructure. The CGI graphites are elongated, randomly oriented and interconnected, as they are in LGI, however they have rounded edges and are shorter and thicker. These characteristics provides stronger adhesion between graphite and matrix which results on CGI improved mechanical properties. [2]

The microstructure of CGI also presents nodules and, as nodularity increases, CGI's mechanical properties increases as well. [2] However, a high nodularity, along with other solidification characteristics, leads to one of the main challenges in CGI production, it reduces the material castability and one of the reasons is the increase in shrinkage porosity tendency along with increase of nodularity.

Therefore, it is very important to understand how the nodules forms during solidification. But not only nodules seems to be influencing shrinkage porosity formation in CGI, recent studies have shown that it is possible to relate different types of shrinkage porosities to different solidification stages based on the dendrites morphology found inside these porosities. These studies have also shown that the size and distribution of eutectic cells have an important role in shrinkage porosity formation. [3]

1.1 MAIN OBJECTIVE

The main objective of this work is to increase the knowledge about microstructure formation in CGI during solidification, how it influences shrinkage porosity formation.

1.2 SPECIFIC OBJECTIVES

In order to achieve the main objective, the following specific objectives are set:

- To cast a specimen, susceptible to shrinkage porosity formation, with different combinations of magnesium content and inoculation level.
- To study the internal surface of the porosities found and relate it to the moment they form during solidification.
- To evaluate the influence of this combination of parameters on the occurrence of shrinkage porosities by understanding how they influence the microstructure of the specimens. The aspects under evaluation includes nodularity, size and distribution of eutectic colonies at specific regions of the specimen and the microstructure formed between these regions.

2 LITERATURE REVIEW

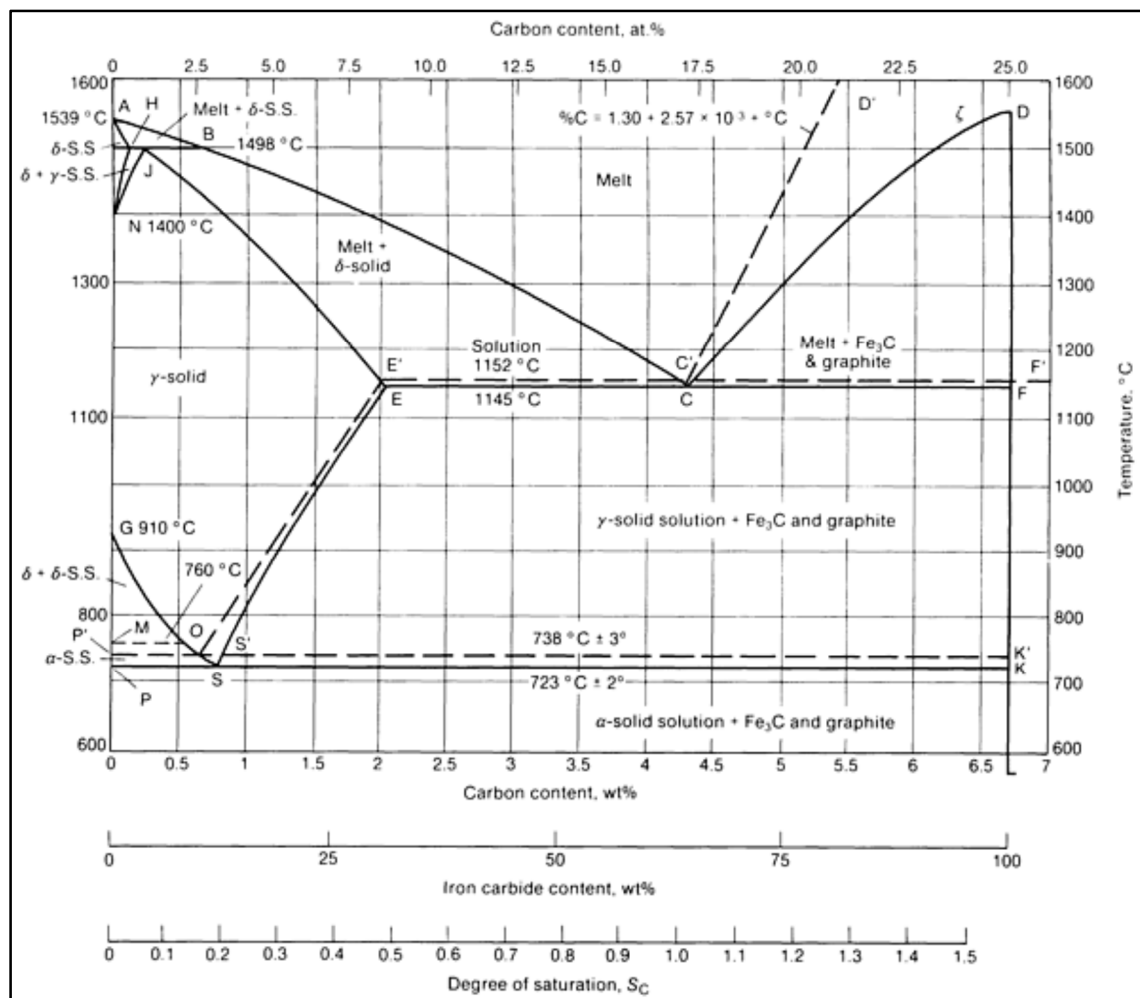
This section reviews some important theoretical concepts found in technical literature in order to facilitate the understanding of the work and introduce the reader to compacted graphite iron and some problems associated with casting process. It starts with the introduction of cast iron, including CGI production, following with an explanation of cast iron solidification, and finishing with the introduction of shrinkage porosity formation in cast iron.

2.1 CAST IRON

Cast iron is, in general, a multi-component alloy consisting mainly by Fe-C-Si, typically C between 2 and 4% and Si between 1 and 3%. Figure 1 shows the iron-carbon diagram, which is a very important tool for study and comprehension of cast iron microstructure evolution during solidification. [4] [5]

According to the diagram, carbon contained in cast iron precipitates during solidification by an eutectic reaction either as a stable graphite phase (graphite iron) or a metastable cementite phase (white iron) or even a mixture of those two (mottled iron). Which phase will be precipitated during solidification depends on factors such as graphitization potential of the liquid, inoculation treatment and cooling rate. [4] [5].

Figure 1 – Iron-carbon diagram. The dashed line represents the stable diagram and the solid line represents the metastable diagram



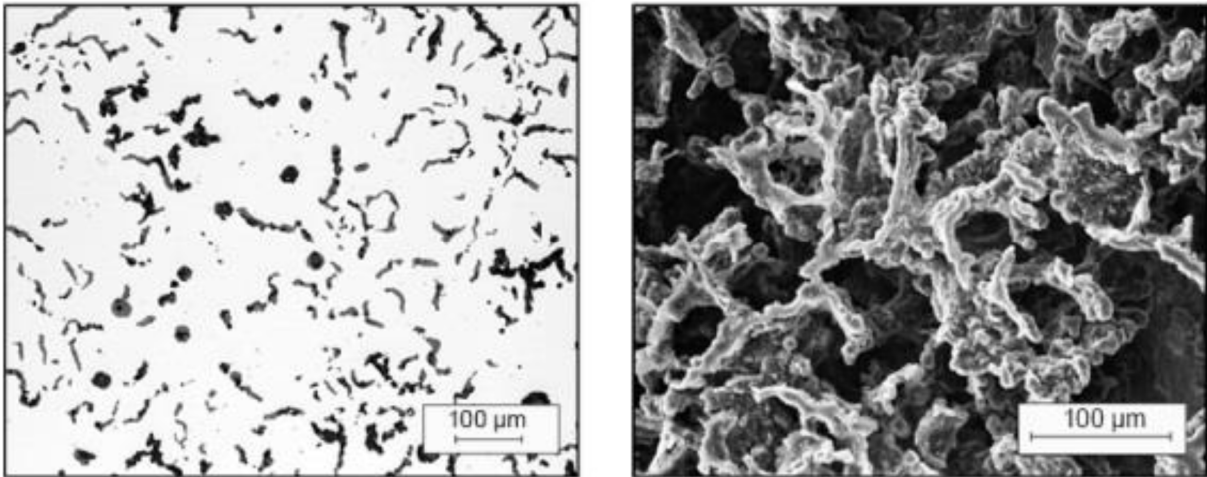
Source: ASM 2008

2.1.1 Compacted graphite iron (CGI) production

Compacted graphite iron has been first produced non-intended in the past, by using insufficient magnesium or cerium levels during SGI production. Only since 1965 that CGI was placed among the cast iron family as a material with distinct properties, with the first patent obtained by R.D. Schelleng. [6] [4]

An acceptable CGI cannot have any flake graphite present in its microstructure and the amount of spheroidal graphite cannot exceed 20%. Therefore, 80% of all graphite must be compacted, ASTM A 247, type IV. Figure 2 shows a typical CGI microstructure.

Figure 2 – Typical CGI microstructure. Left - CGI with 10% nodularity. Right - Deep etch SEM micrograph of a compacted graphite.

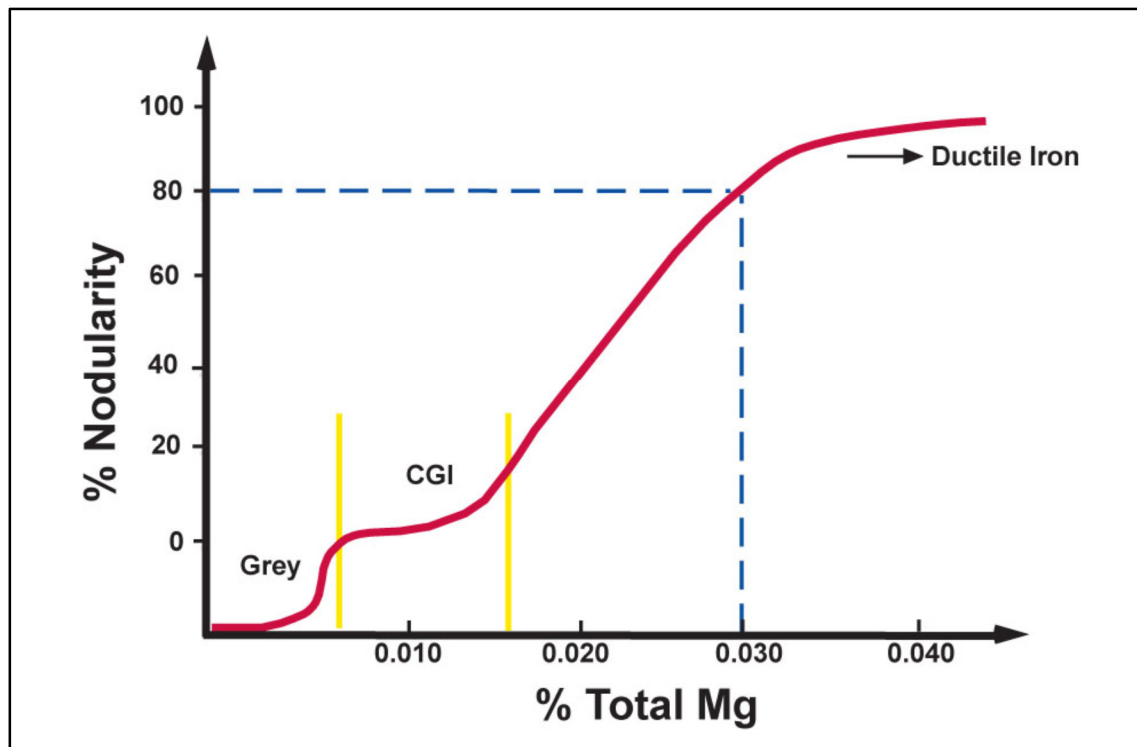


Source: DAWSON AND INDRA 2007

In order to obtain compacted graphite it is necessary to use a nodularization treatment, as used for SGI production. Common elements used for this treatment are magnesium, rare earths (cerium, lanthanum, and others) and titanium (as an anti nodularization element). The amount of nodularization element added to the melt during nodularization treatment must be strictly controlled in order to obtain a CGI microstructure with maximum 20% of nodules.

Figure 3 shows an example of composition range for Mg as nodularization element. If too much magnesium is added during treatment, the amount of nodules in the microstructure will rise and the material will solidify with a SGI microstructure. If there is not enough magnesium, the material will solidify with a LGI microstructure. The figure shows that there is an abruptly change in the microstructure from CGI to LGI at approximately 0.006% Mg. [7]

Figure 3: Composition range for use of Mg for a stable CGI production, for a base iron that contains 0.010-0.015% sulfur. [7]



Source: DAWSON, 2002

Despite the fact that figure 3 shows a stable range of approximately 0.010% Mg, in practice, this range is much smaller and one of the reasons is that active Mg fades at a rate of approximately 0.001% every five minutes. Therefore, at the beginning of pouring the amount of active Mg at a ladle cannot be close to the compacted to lamellar microstructure transition, in order to avoid formation of lamellar graphite before the end of pouring of that ladle. [7]

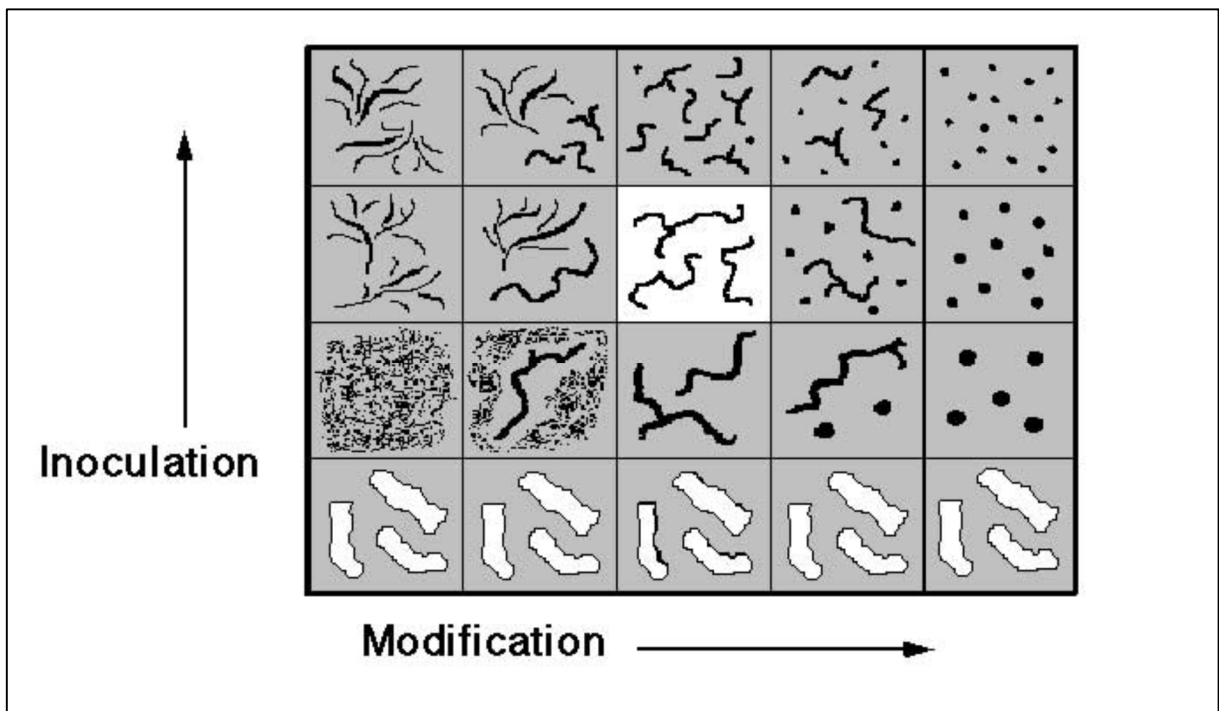
The amount of sulfur at the bath also increases Mg fading rate, limiting the amount of sulfur in base iron for CGI production to less than 0.020%. One way of counter acting this effect would be to increase Mg addition as used for SGI, however an over addition of Mg to CGI would increase the nodularity beyond the 20% specified limit and could also lead to porosity defects generation. [7] The Mg working range for SGI is approximately 0.020%, from 0.030 to 0.050%, while for CGI this range drops to approximately 0.002%, from 0.012 to 0.014%.

The use of rare earths such as cerium in addition to magnesium as a nodularization agent also increases the stable plateau for CGI production since rare earths are less volatile than magnesium, are not as potent as magnesium in increasing

nodularity and tend to form more stable sulfides and oxides, reducing fade rate. [8] The use of rare earths, not as the main nodularization agent but as an aid, helps to reduce their negative effect of acting as a strong carbide promoter, especially in small castings or thin-wall castings that have fast solidification rates. [8]

Nodularization agents are not the only parameter involved in the production of CGI since inoculation addition also plays an important role in it. According to figure 4, inoculation addition to CGI causes a nodularity increase, as it facilitates the formation of graphite nuclei during solidification. [7]

Figure 4: Influence of Inoculation and Modification (through magnesium addition) over CGI microstructure.



Source: DAWSON, 2002.

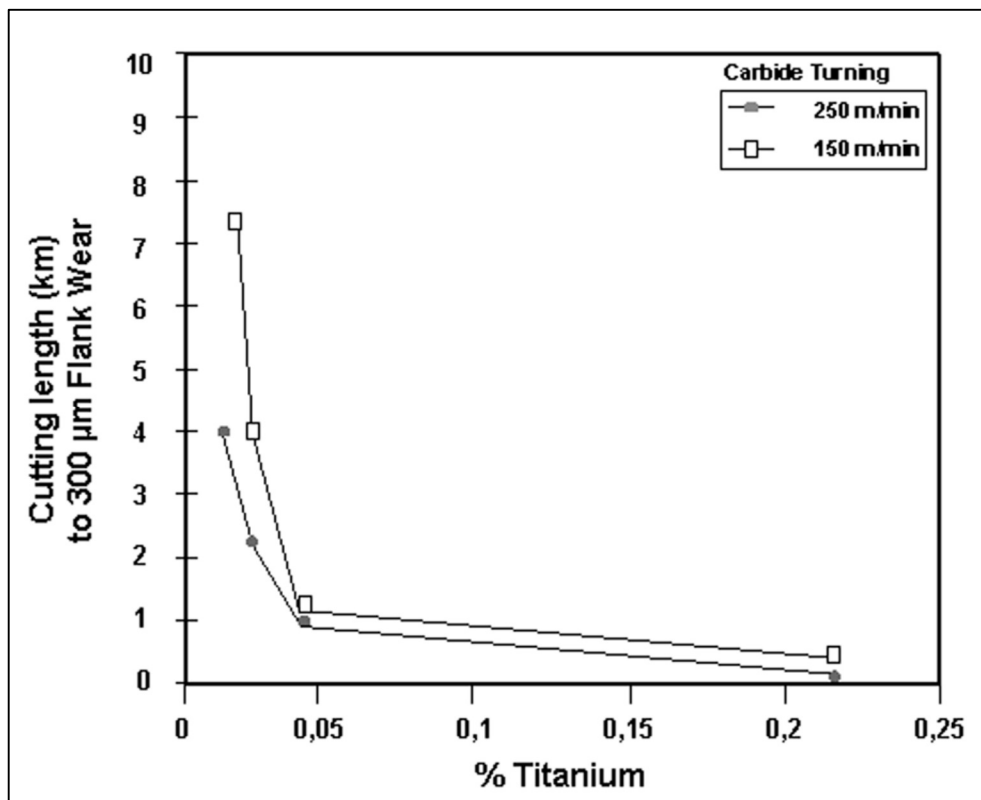
An alternative way to increase CGI process stability is to use titanium additions to the melt since it prevents the formation of nodular graphites in the microstructure, which increases the stable range of magnesium during process. However, studies have shown that an increase in titanium from 0.01 to 0.02% reduces the tool life in machining operation by approximately 50%. [9]

Figure 5 shows the decrease in tool life caused by titanium addition, this drop in tool life observed in the figure was also observed recently by other authors that found a decrease of about 2.5 times in tool life when the titanium content was increased from

0.005 to 0.03%. [10] The reduction in tool life decreases the machinability of the parts produced using titanium; Therefore, while parts that are subjected to limited machining operations such as exhaust manifolds and brackets tolerates the use of titanium, [9] it is not possible to use this process route for the production of intensive machining parts such as cylinder blocks and heads. [11]

The production of CGI cylinder blocks and heads was only possible after the invention of liquid metal control processes that allowed the foundries to work within this narrow magnesium range, such as SinterCast, OCC, Novacast and Oxicast. The processes that came before generated too much variations of both composition and microstructure to be used in industrial scale. [12]

Figure 5: Reduction in tool life of CGI during carbide turning caused by titanium addition.



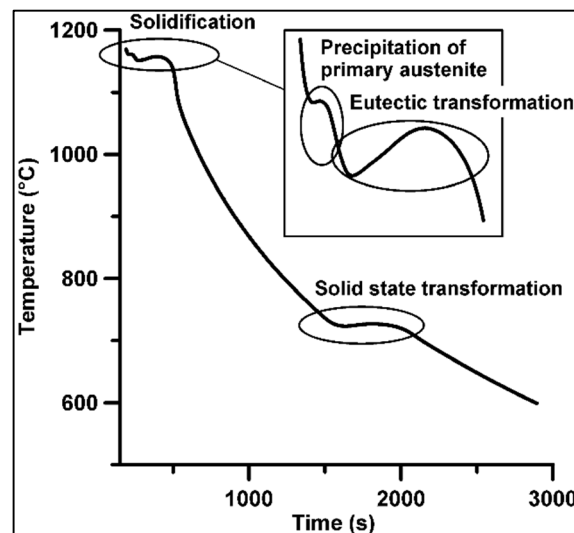
Source: DAWSON, 2001.

2.2 SOLIDIFICATION OF CAST IRON

The iron-carbon diagram, shown in figure 1, shows that the cast iron is an alloy that passes through an eutectic transformation at the temperature of 1152°C, when it solidifies according to the stable diagram, dashed line. The eutectic composition is of approximately 4.3% of carbon. Hypereutectic alloys have compositions with carbon content higher than 4.3% and hypoeutectic alloys have compositions with carbon content lower than 4.3%. For any composition other than the eutectic, the solidification of cast iron starts with the precipitation of the primary phase, which can be graphite, for hypereutectic compositions, or with the precipitation of austenite, for hypoeutectic compositions. [4]

Figure 6 shows a cooling curve obtained during solidification of a hypoeutectic cast iron until below the solid state transformation temperature. The region highlighted at the figure shows the precipitation and growth of primary austenite and the eutectic transformation.

Figure 6: Example of cast iron cooling curve.



Source: KONIG 2011

The understanding of the solidification process is of great importance for the control of iron properties and defect formation. This section aims to review basic concepts of solidification science and to apply them to understand specifically the solidification of cast iron alloys.

2.2.1 Nucleation Process

Primary and eutectic phase nucleation are both heterogeneous nucleation processes. The understanding of this process is limited and the models used to describe it are extensions of the homogeneous nucleation theory. [5]

For the nucleation of a particle occur in a homogeneous melt, where all the components are homogeneously in the liquid phase, a minimum number of atoms must arrange themselves on the sites of the solid crystal lattice. This is possible only for a large undercooling, a large difference between the temperature of the melt and the melting temperature of the metal. For a small undercooling, the probability for the metallic atoms to arrange themselves and form a nucleus is very small. [13]

The reason for this is that small crystals, such as the ones formed at the beginning of a solidification process, tend to form large curvature interfaces due to the atomic dimensions of the newly formed crystal. This large curvature creates a large pressure difference between the crystal and the melt, which lowers the melting point of the recently formed crystal, re-melting it. Therefore, an equilibrium between the curved crystal and its melt must exist in order to start the nucleation process. The crystal must reach what is called the critical radius to stablish this equilibrium, which in a homogeneous melt, requires a large undercooling to happen. [13]

In a heterogeneous nucleation process, the presence of solid particles in the melt or a mold wall, for example, can lower the energy required to start the nucleation as the solid particles present in the melt have good solid/solid wetting with the crystal nucleus, which than require less number of atoms and energy to achieve the critical radius. The inoculation process used in foundries is an application of this phenomenon, where the foundry adds solid particles to the melt in order to increase the nucleation ratio. [13]

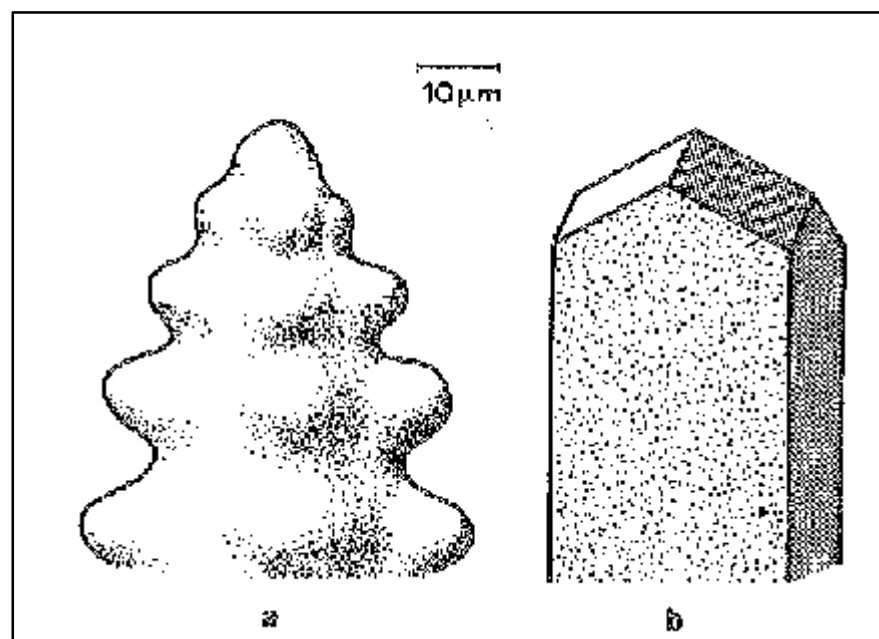
2.2.2 Growth Process

After nucleation, the next step of the solidification is the growth process where there is transference of atoms from the liquid to the nucleus at the solid-liquid interface. Therefore, the structure of the solid-liquid interface and solute gradients formed in the liquid at the interface are very important for the solidification. [5]

There are two types of solid-liquid interfaces, atomically smooth and atomically rough. Materials with high entropy of fusion presents smooth surfaces with limited number of sites for atomic addition during growth. If there is no defects on the structure, it is necessary to form a stable interface to result in a growth step and this must be repeated for every step requiring a certain undercooling to sustain the growth. When there are defects such as screws dislocation a self-driven growth process is established and the undercooling required to sustain growth is reduced. Materials with this solid-liquid interface have a considerable anisotropy of growth that results in faceted structures, such as the graphite phase in cast iron. [5]

Many of the common metal presents a rough solid-liquid interface and presents non-faceted growth forms, with both undercooling and growth rate anisotropy being smaller when compared to smooth surfaces. During solidification atoms joins the growing surface at any point and capillary effects and diffusion of heat and/or solute mainly determine the shape of the crystal. There is still a slight anisotropy of growth in these crystals and it leads to the formation of dendrites arms in specifics crystallographic directions. Figure 7 shows examples of faceted and non-faceted growth morphologies. [5] [13]

Figure 7: Non-Faceted (a) and faceted (b) growth morphologies.



Source: KURZ & FISCHER 1992

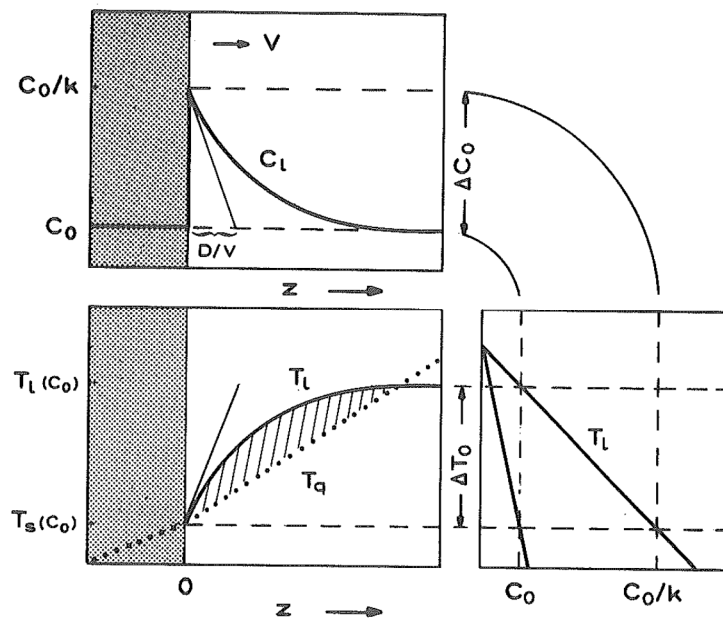
2.2.3 Constitutional undercooling

During growth, the solid phase will eject elements to the liquid phase due to their smaller solubility in the solid phase. This will cause an enrichment of solute in the region ahead of the solid-liquid interface and affect the solidification temperature of the liquid, T_l , in this region, which relates to the composition through the following equation:

$$T_l(C_0) - T_l = m(C_0 - C_l)$$

Where $T_l(C_0)$ is the liquidus temperature of the initial alloy composition. Figure 8 shows this relationship. [13]

Figure 8: Illustration of the constitutional undercooling in alloys.



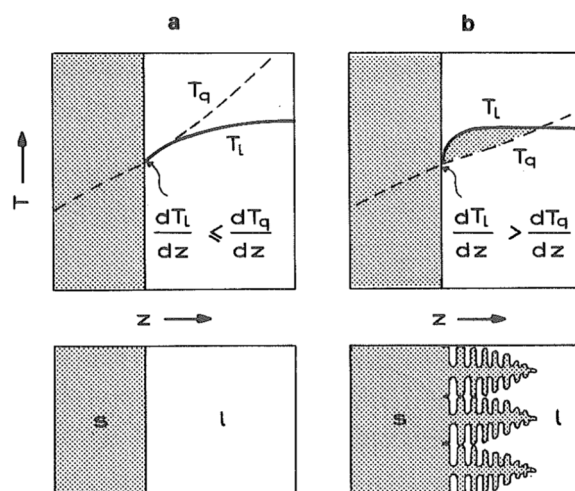
Source: KURZ & FISCHER 1992

As the liquid concentration decreases, shown in the upper left diagram in figure 8, the liquidus temperature T_l , of the liquid ahead of the solid-liquid interface increases, as shown by the lower left diagram. However, each volume within the region with decreasing concentration is submitted to the temperature imposed by the heat flux T_q . To maintain the driving force for the atomic addition mechanism, T_q must be lower than the solidus temperature T_s , this means that the liquid ahead of the solid-liquid interface, with high solute concentration and liquidus temperature gradient higher than the heat

flux gradient is thus undercooled. The dashed region in the diagram represents this liquid volume and is known as the constitutional undercooling. [13]

Figure 9 shows the difference between a stable and an unstable solid-liquid interface using the constitutional undercooling concept, in (a), the liquid temperature gradient is below the heat flux gradient at the region ahead of the solid-liquid interface and it is stable, forming a planar growth interface. In (b), the liquid temperature gradient is above the heat flux gradient at the region ahead of the solid-liquid interface, the liquid is undercooled by the increase in solute concentration. This is a driving force for interface change, undercooling increase as the tip of the perturbation advances into the melt, therefore the interface is unstable, and the dendritic structure can form. [13]

Figure 9: Growing surfaces with and without constitutional undercooling at solid-liquid interfaces.



Source: KURZ & FISCHER 1992

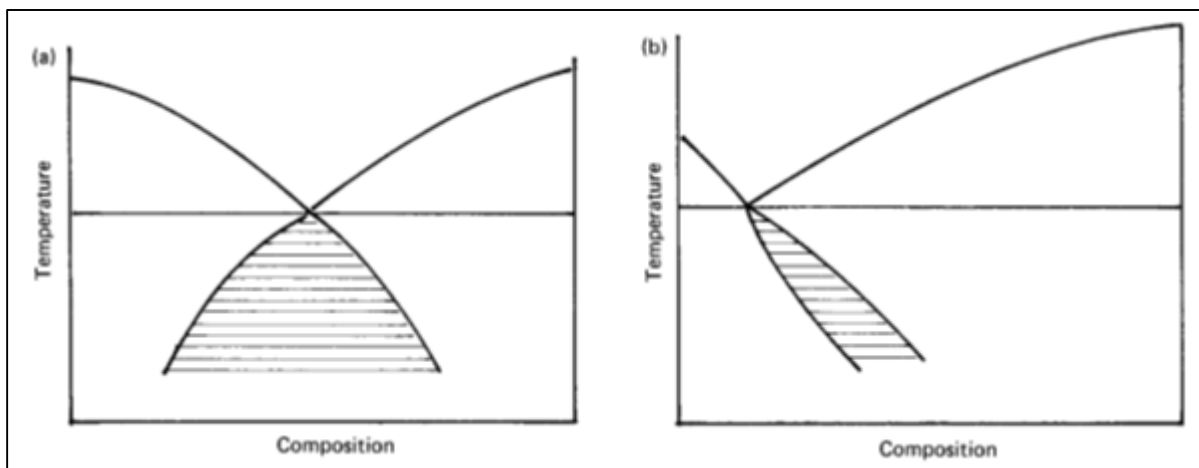
2.2.4 The Coupled zone

The coupled zone concept explains why there is formation of primary austenite in irons of eutectic and slightly hypereutectic compositions and the formation of an austenite halo around primary graphite. It also explains why the amount of undercooling influences the amount of primary austenite formed in the alloy during solidification, which affects both contraction during solidification and final mechanical properties of the material. This zone defines the conditions under which two different eutectic phases can grow having the same interface at a rate higher than that each

phase separately. The growth characteristics of the two phases and the solidification condition determines the shape of the coupled zone. [5] [13]

Figure 10 shows typical coupled zones for isothermal growth. Diagram (a) shows a typical shape of the zone formed by a normal eutectic alloy, when both eutectic phase grow in a non-faceted manner. Diagram (b) shows a typical shape of the zone for an anomalous eutectic alloy, with one eutectic phase growing with a non-faceting behavior and the other with a faceting behavior. [5]

Figure 10: Typical coupled zone shapes for normal eutectic alloys (a) and anomalous eutectic alloys (b) for an isothermal growth condition.



Source: ELLIOTT 1988.

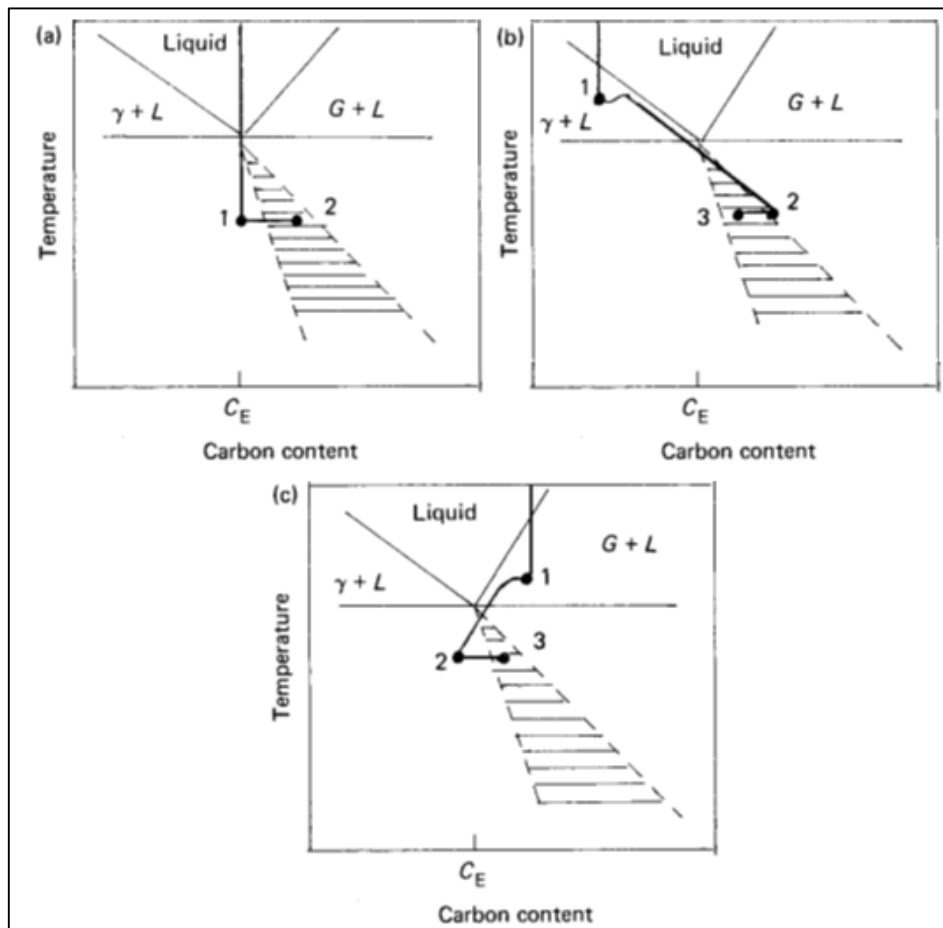
Cast irons belong to the anomalous group of eutectics. Figure 11 shows the solidification behavior for a LGI, related to the coupled zone, with eutectic, hypoeutectic and hypereutectic composition. The eutectic alloy solidification begins with nucleation when the alloy undercools to the point 1, in the diagram (a). The location of point 1 is outside the coupled zone, at this position the austenite growth rate is higher than that of the eutectic or the graphite, therefore it nucleates more easily and austenite dendrites starts growing in the liquid. As the dendrites grows they enrich the liquid in the interdendritic areas in C, reaching the composition in point 2, as this point lies inside the coupled zone, the austenite graphite eutectic forms. [5]

The hypoeutectic solidification starts with the nucleation of austenite at point 1 in diagram (b). As the dendrites grows they enrich the liquid in the interdendritic areas in C, reaching the composition in point 2, where graphite starts to nucleate, this takes

the composition to the point 3, inside the coupled zone where the austenite graphite eutectic starts to form. [5]

With hypereutectic composition, the nucleation of primary graphites starts at point 1 in diagram c. As the graphites grows, the liquid metal in the areas surrounding it become depleted in C, leading the local composition to point 2 where austenite nucleates and grows as a halo around the primary graphite. The formation of this halo segregates C to the liquid reaching the composition in point 3, inside the coupled zone and the eutectic solidification continues in the same way as in a liquid of eutectic composition. [5]

Figure 11: Solidification paths for LGI of eutectic composition (a), hypoeutectic composition (b) and hypereutectic composition (c), using the coupled zone concept.



Source: ELLIOTT 1988

Figure 11 shows that, with a higher undercooling, more primary austenite will form before the eutectic starts to nucleate at the coupled zone. As it will be discussed in more details in section 2.3, a higher volume of dendrites in the microstructure

increases the probability of shrinkage porosity formation in cast iron, since it is harder to fill liquid metals through the dendritic arms during solidification. [13]

2.2.5 Austenite Primary Phase Formation in Cast Irons

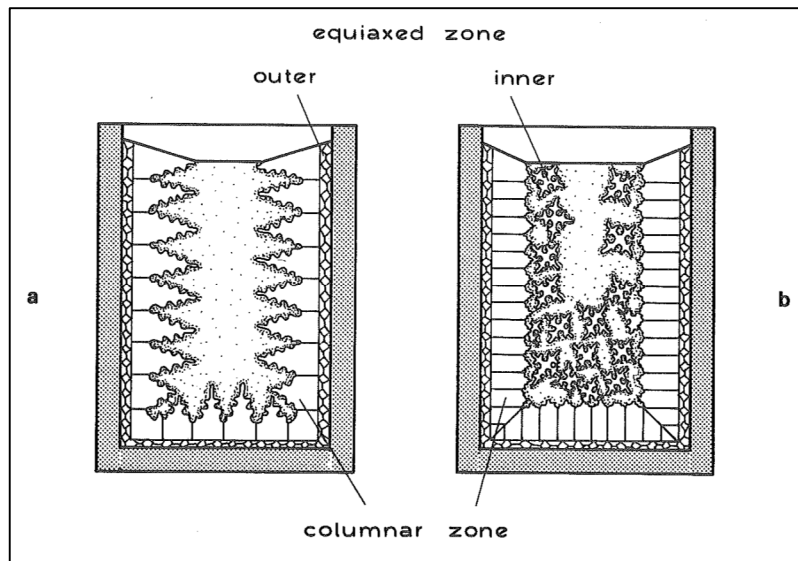
According to solidification theory, the formation of the primary austenite in cast iron starts with nucleation of small crystals close to the mold wall. These crystals increase in size following a typical non-planar solidification front, resulting in a dendritic microstructure, which grows in a direction parallel and opposite to the heat flow, in this case, the heat flows in a direction towards the mold wall. When other growing directions are outgrown by mutual competition, a columnar zone is formed. [13]

Continuing the solidification, some branches of the dendrites starts to detach from the latter and starts growing in an equiaxed shape. At the same time, other equiaxed grains starts to nucleate on particles or impurities floating in the melt. At these crystals, the heat is extracted radially by the undercooled melt, which is colder than the crystals. [13] While these crystal grows they move freely in the melt until a solid skeleton is formed. [14]

As the nucleation phase ends at the maximum undercooling and the number of nuclei had reached its maximum value, the growth phase starts, being marked by an increase in temperature known as recalescence. [15] The growth of the crystals ends when they start to impinge in each other, blocking further growth. This point is defined as the coherence point, from this moment on, the solidification continues with dendrite coarsening. [16] As the coherence point happens when the equiaxed dendrites impinge with the columnar dendrites, it also defines the columnar to equiaxed transition point.

Figure 12 illustrates the formation of both columnar outer zone and equiaxed inner zone by the primary dendrites of austenite. [13]

Figure 12: Formation of primary structure during solidification.



Source: KURZ & FISHER 1992

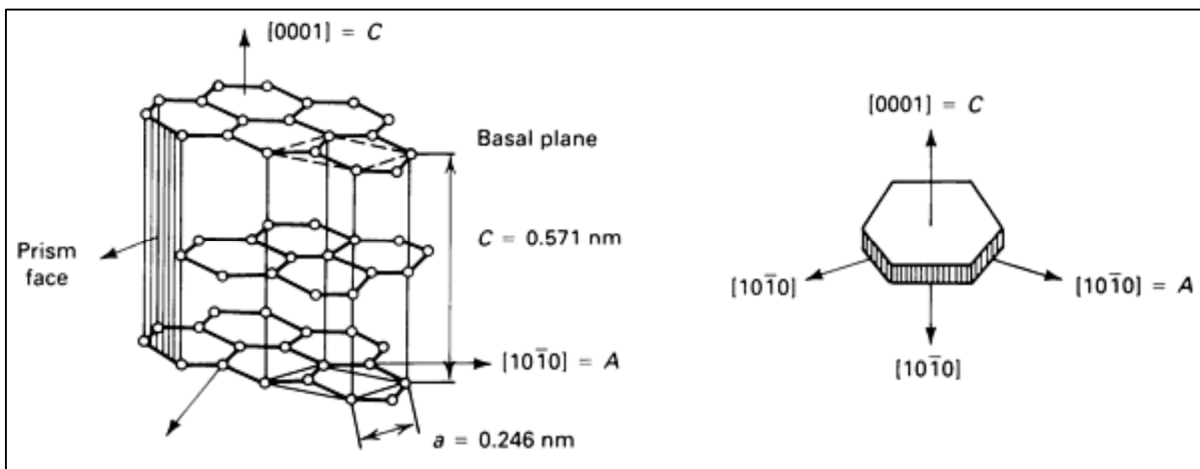
In cast irons, during the dendritic growth, the dendrites eject carbon into the melt through the solid/liquid interface and the content of carbon in the liquid increases, along the liquidus line, shown in the phase diagram in figure 1. When the liquid composition reaches the eutectic composition, at carbon content of 4.3%, and the temperature drops below the eutectic transformation temperature, approximately 1152 °C, the eutectic cells start to nucleate. [4]

2.2.6 Eutectic Formation in Cast Irons

The eutectic solidification starts when the temperature falls below the eutectic transformation temperature shown in the phase diagram, figure 1, with the nucleation of both graphite and austenite from the remaining liquid. For this nucleation to occur a determined amount of undercooling is required. [13]

When analyzing the graphite structure for the different cast iron grades it is possible to see that the lamellar graphite grows predominantly along the *a* direction and the spheroidal graphite grows predominantly in the *c* direction with a radial stacking of the basal plane. The compacted graphite shows a different behavior with the graphite growing sometimes in the *a* direction, similar to the lamellar graphite and sometimes in the *c* direction, in a radial manner similar to the spheroidal graphite. [17] Figure 13 shows the graphite unit cell.

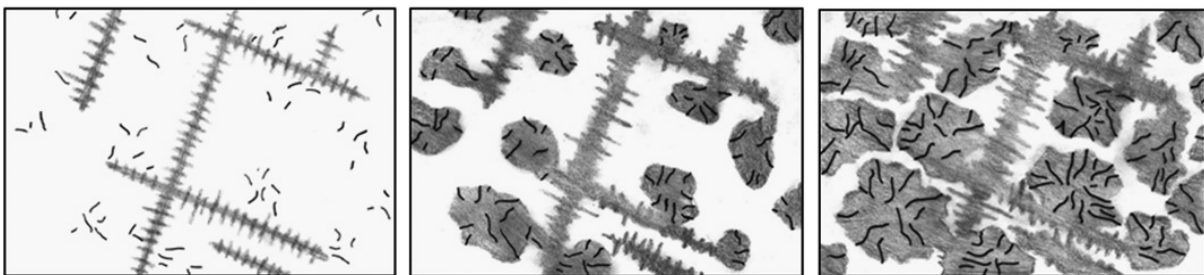
Figure 13 – Hexagonal structure cell of the graphite, showing the basal plane and prismatic face and the a and c directions. [18]



Source: Minkoff 1983.

For LGI, eutectic solidification is said to be cooperative, with the graphite growing in direct contact with the liquid, forming an eutectic cell. [19] Recent studies have also proposed that, for an eutectic composition, the lamellar graphite nucleates in the melt at the same time as the austenite does and as heat is extracted from the melt, austenite dendrite grows and start to interact with graphite particles, than forming the eutectic cells that grows cooperatively. [20] Figure 14 show a schematic of the proposed eutectic formation.

Figure 14: Schematic of the eutectic growth in LGI.

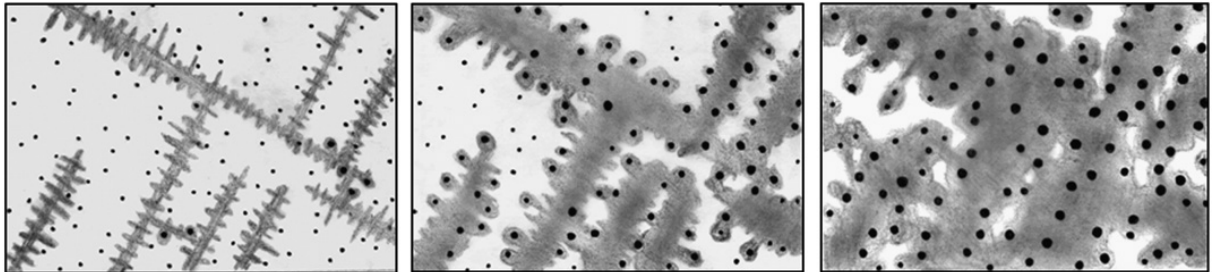


Source: Rivera 2008.

For the spheroidal graphite iron (SGI), studies have proposed that the solidification of the eutectic also begins with the nucleation of graphite and austenite independently. However, for SGI, as the austenite grows it envelopes the graphite particles and then the remaining growth is controlled by diffusion of carbon through the austenite shell while the secondary arms of the austenite continue to grow and

coarsen. The process finishes with the solidification of isolated pockets of interdendritic melt. [19][20][21][22] Figure 15 show a schematic of the proposed eutectic formation.

Figure 15: Schematic of the eutectic growth in SGI.

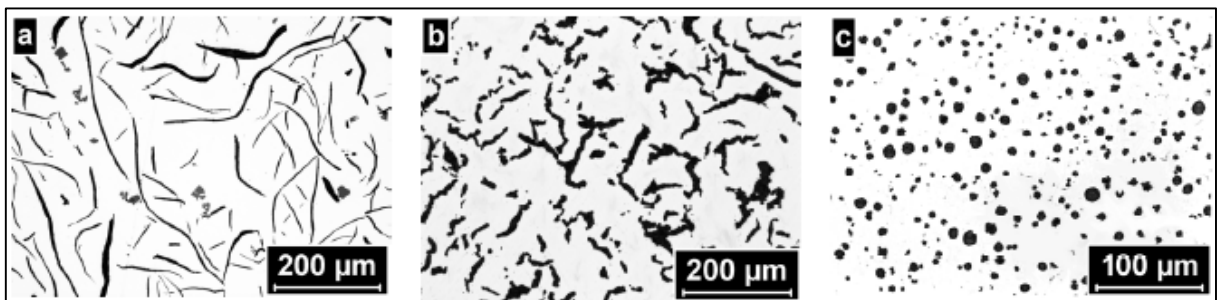


Source: Rivera 2008.

In a similar manner to LGI, the solidification of CGI occur with the graphite growing in contact with the melt, however this contact is not as direct as in the case of LGI. The compacted graphite remains in contact with the melt only through thin liquid channels until austenite envelopes it, finishing the solidification in a similar way to SGI, with the solidification of isolated pockets of interdendritic melt. [23]

Figure 16 shows the different graphite morphology presented by the three classes of cast irons.

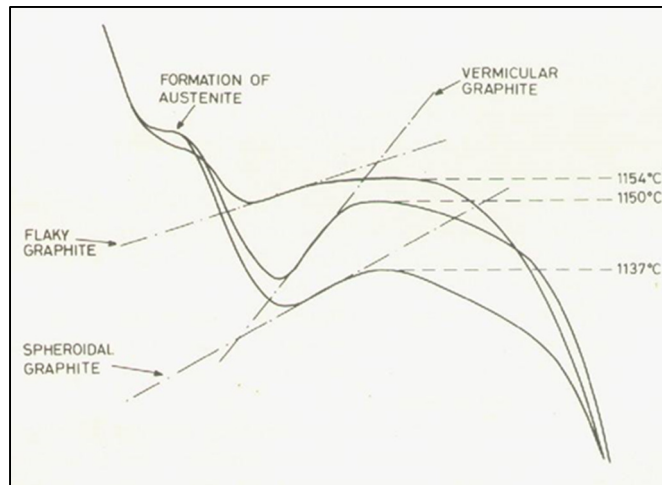
Figure 16: Cast iron different graphites morphology. a. LGI, b. CGI, c. SGI.



Source: KONIG 2011.

Due to the growth conditions, CGI presents a high undercooling during solidification, which can achieve temperatures below the eutectic metastable transformation temperature; this makes this material susceptible to carbide formation. [24] Figure 17 shows cooling curves, obtained using a metallic thermal analysis cup, for the different types of cast iron where it is possible to see that both CGI and SGI have higher undercooling when compared to LGI. [25]

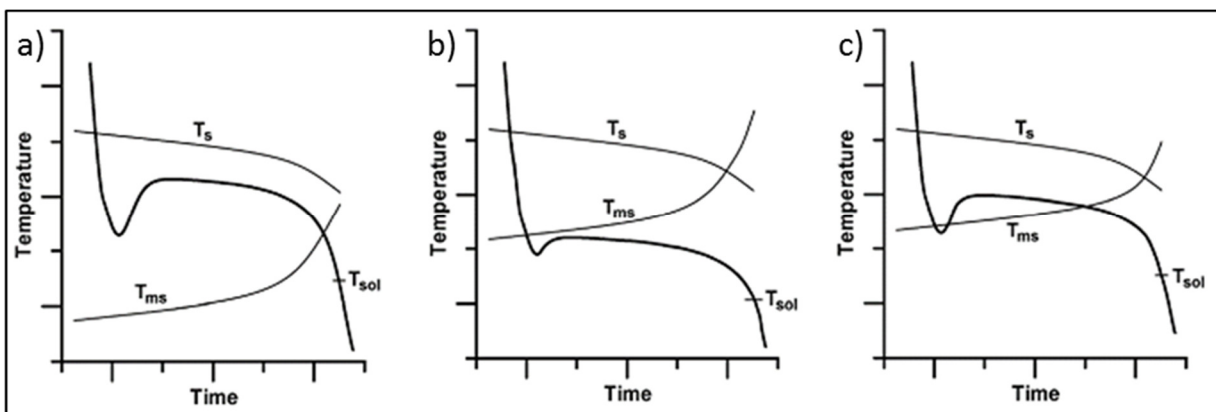
Figure 17: Cooling curves for three types of cast irons obtained with metallic cup.



Source: BÄCKERUD, 1975

Figure 18 shows different conditions for carbide formation during solidification of CGI. It is important to notice that both eutectic transformation curves are not isothermal due to the segregation of elements to the last to freeze liquid, resulting in carbide formation at the end of solidification, as shown in the graphic a) of figure 17. A slow cooling rate with low numbers of growing grains can lead to this cooling profile. [26] [27]

Figure 18: Conditions for carbide formation. a) Segregation carbides. b) Chill carbides. c) Mottled structure.



Source: KONIG 2011

Figure 18 b) shows a solidification with high cooling rate such that the solidification will occur below the metastable eutectic transformation temperature, resulting in a white structure after solidification. Thin sections of the casting presents this type of microstructure more often. [28]

The graphic c) in figure 18 shows a solidification that mixes the behavior of the two previous curves. The undercooling temperature drops below the metastable transformation temperature but then rises above it due to the recalescence and finishes again below the metastable temperature. This generates the mixed microstructure known as mottled iron. [28]

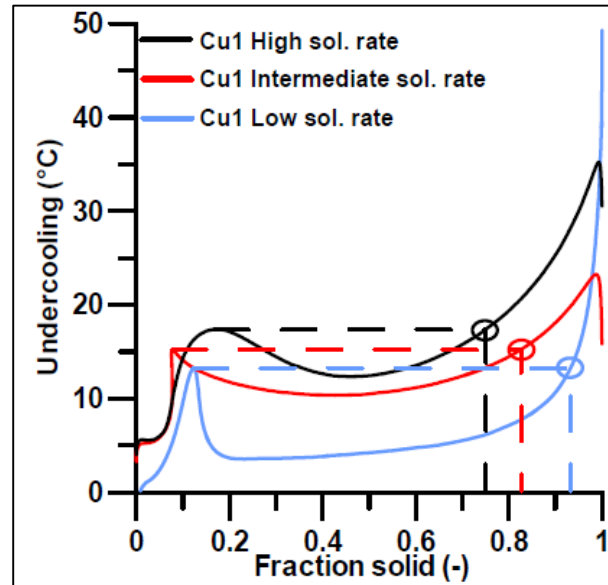
A study on microstructure formation in CGI has shown that the increase in nodularity by the increase in nodularization elements also increases the carbide formation tendency. It is proposed that the solidification with high amounts of nodularization agents would cause the solidification of CGI to happen in a similar manner to SGI solidification, which without the over inoculation commonly used for SGI, would result in a higher chilling tendency. [28]

The presence of carbide forming elements in the melt also increase the chilling tendency of CGI, comparing the influence of different elements such as Cr, Mn and Mo, the study has showed that Mo have generated greater chilling tendency in CGI melts. [27] Regarding graphite promoters, copper would have the most significant influence in reducing chilling tendencies when compared to Si and Sn. It is important to observe that during the experiment the amount of carbon was reduced for high silicon series in order to keep the carbon equivalent constant, what could have reduced the influence of this element in preventing carbide formation. [28]

2.2.7 Double population of eutectic cells and nodules

The nucleation of eutectic cells in two different stages of solidification was identified during a CGI microstructure formation study conducted by Konig [25]. The first during maximum undercooling, prior to recalescence and the second at final part of solidification when the temperature reaches the maximum undercooling temperature after recalescence, figure 19.

Figure 19: Undercooling as a function of fraction of solid for a CGI series of experiment with varying cooling rates. The graphic shows, within the circles, when the secondary eutectic cells nucleation starts regarding undercooling.



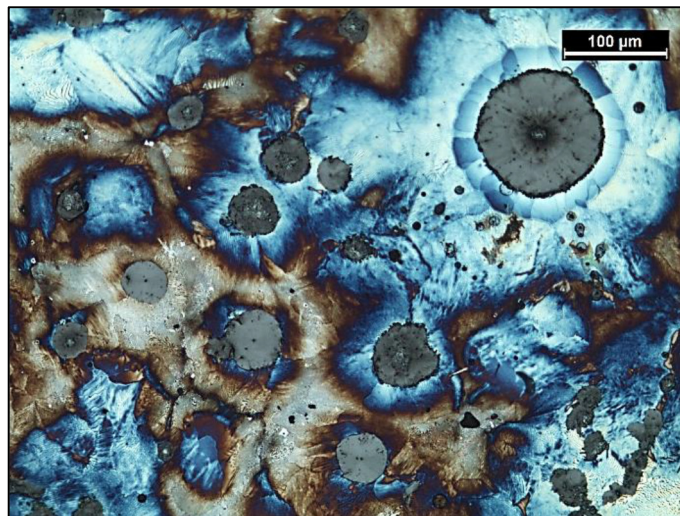
Source: KONIG 2011

Konig's work [2011] has proposed that the nucleation rate influences the area fraction occupied by eutectic grains in the microstructure of CGI. A higher nucleation rate would initiate the second nucleation of the eutectic at a lower fraction of solid, which means that the secondary eutectic cells would stop the growing of the primary eutectic cells at an early stage, resulting in smaller eutectic cells in the final microstructure. [28]

For SGI, there is a bimodal distribution of nodules often found in eutectic and hypereutectic compositions. In hypereutectic compositions the larger nodules are explained as being primary nodules that had more time in contact with the liquid before the austenite envelopes it and reduces the growth rate. [29] This same bimodal distribution of nodules have been reported qualitatively for CGI. [28] [3] [32]

The larger set of nodules are not only distinguished by their size but they are usually surrounded by a silicon rich shell of ferrite, while the smaller set of nodules are usually surrounded by pearlite or just a little of ferrite and are located in last to freeze areas between the eutectic cells. [28] [3] [32] Figure 20 shows the two types of nodules in a CGI microstructure.

Figure 20: Image showing double population of nodules. Large nodule within a ferrite shell and smaller nodule with small or no ferrite shell precipitated in last to freeze area.



Source: VAZEHRAD 2011.

2.2.8 Microsegregation

Carbon is not the only element in cast iron that segregates. The main alloying elements in cast iron segregates, such as silicon and manganese. An important tool to understand segregation is the partition coefficient, K usually defined as:

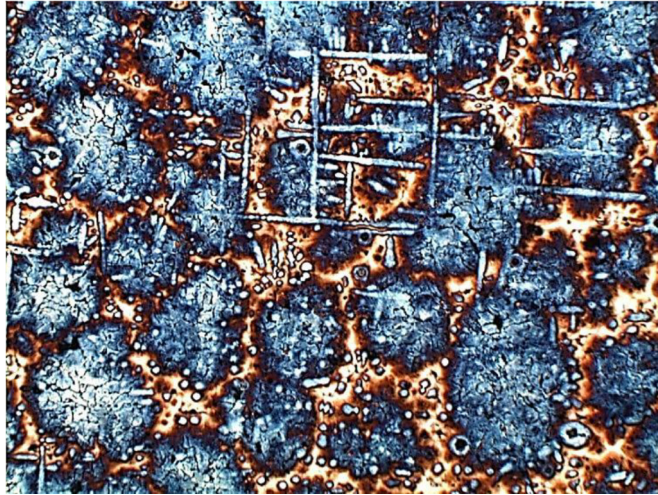
$$K = \frac{C_s}{C_l}$$

Where C_s is the concentration of the element in the solid and C_l , the concentration in the liquid. The elements that presents $K > 1$ are said to have an inverse segregation pattern and segregates to the first regions during solidification, Si and Cu have this behavior. Elements that presents $K < 1$ are said to have a direct segregation pattern and segregates to the last regions to solidify; P, Mn, Cr, Mo and Mg have this behavior [13] [7].

The segregation pattern of cast iron is very important for the study of solidification and it can be revealed using color etching techniques. [30] Figure 21 shows a typical microstructure revealed using color etching for a CGI sample. Areas with blue color represents high silicon segregation and the light brown areas correspond to low silicon. Since silicon has an inverse segregation pattern it is possible

to conclude that blue regions represents first to solidify areas while light brown correspond to last to solidify areas [28] [3].

Figure 21 – Typical CGI microstructure revealed using color etching. [32]

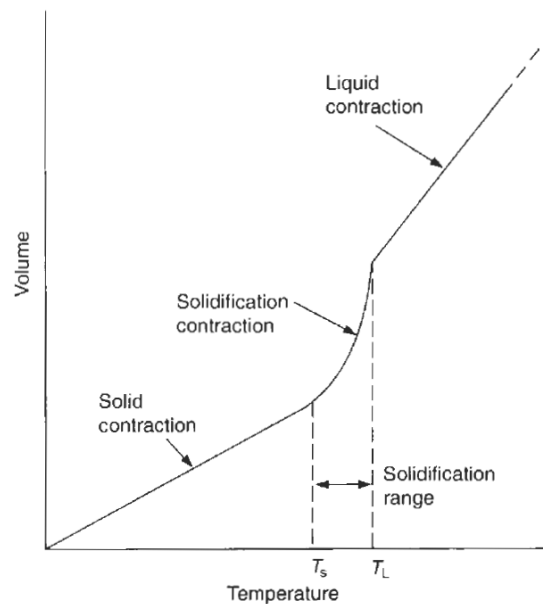


Source: VAZEHRAD, 2011

2.3 SHRINKAGE IN CAST IRON

Among the more challenging types of casting defects occurring in cast irons are the defects related to volumetric changes during solidification. One of these defects is shrinkage, which is a recurring problem for casting manufacturers.

Figure 22: Schematic illustration of the three different contraction during cooling. 1) Liquid Contraction 2) Solidification contraction 3) Solid contraction



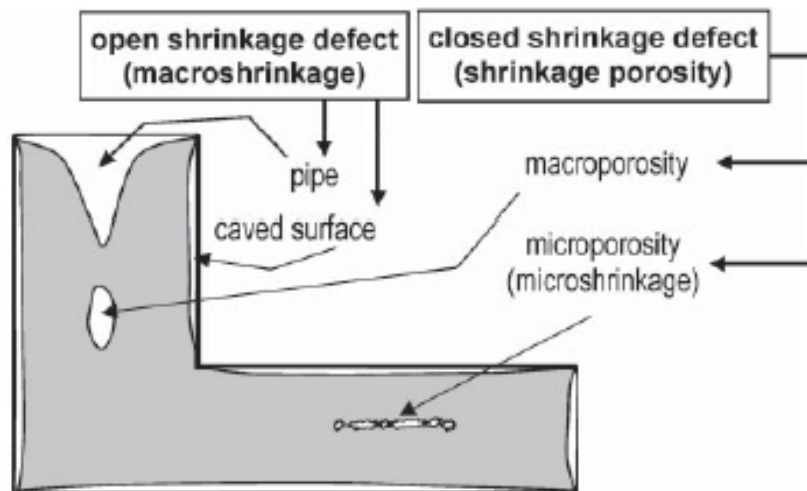
Source: CAMPBELL 2003.

Figure 22 shows the cooling of a liquid metal to room temperature, there are three distinct contractions worth noticing. The first one occurs while the liquid is still cooling and the shrinkage of the metal at this phase is generally occurring while the mold is still being filled. The second contraction occurs at the freezing point, due to the generally greater density of the solid phase compared to the liquid, it is at this contraction that the shrinkage porosity occurs. The third contraction is the solid contraction, where the casting assumes its final shape. Solid contraction must be considered during the design of the pattern in order to achieve the right geometry; other problems that can arise due to this contraction can be concave and distorted surfaces. [33] [34]

The casting soundness depends on the feeding of liquid metal to compensate all contraction submitted to a cast part during solidification. The failure to feed these

regions properly is what causes shrinkage defects formation. Figure 23 shows some definitions and classification of shrinkage defects. [34]

Figure 23: Shrinkage defects classification.



Source: STEFANESCU 2005.

The metal contraction in liquid state and during solidification drives the formation of open shrinkage defects as the ones shown in figure 22, this type of defect can be avoided by the use of correct risering system, which can provide a source of liquid metal to feed the contracting metal. Closed shrinkage defects formation depends not only on metal contraction but also on the pore nucleation and growth inside the casting. [34]

The second contraction has some particularities for cast irons. In LGI, the dendritic solidification facilitates the appearance of voids between the dendritic arms and, as the dendrites coarsen, these voids becomes isolated. [34] Even the precipitation of graphite, which generates a volumetric expansion due to differences between the densities of graphite (2.2 kg/dm^3) and the liquid iron (6.9 kg/dm^3) [33], may not be enough to fill these voids formed between the dendrites arms, due to this isolation behavior [36].

In the case of CGI, the interaction between the graphite and the liquid metal is only between thin liquid channels, the graphite expansion effect is even less than it is for LGI. [41] This graphite growth mode is one of the reasons why CGI is more prone to shrinkage porosity formation when compared to LGI.

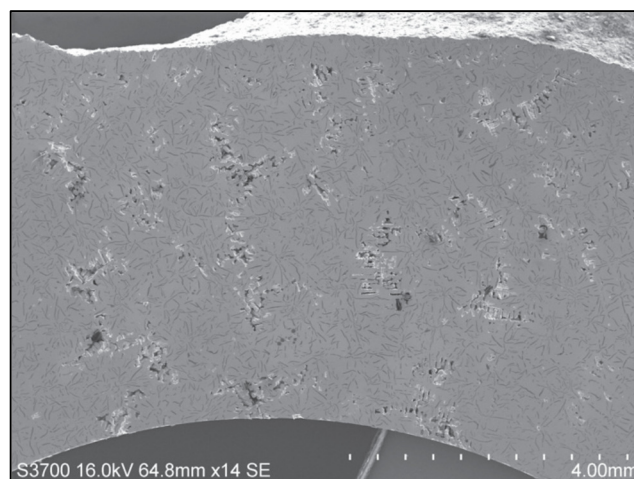
During the solidification of SGI the graphites are enveloped by austenite as soon as the austenite dendrites touches them, thus the austenite network absorbs most of the graphite expansion during the solidification process, transferring it to the mold walls. The austenite network also leaves significant amount of melt between the dendrite arms. These two aspect makes SGI's tendency to form shrinkage porosity bigger than both LGI and CGI. [38] [39]

2.3.1 Shrinkage porosity

Shrinkage porosity is a closed shrinkage defect, leading to internal porosities on castings. It can be classified as macro or microporosity, depending on its geometry, figure 22; microporosity appears in a small scale and can be interconnected with other microporosities forming a network inside the casting. [40] Macroporosity appears as an isolated void in a bigger scale. [36]

Figure 24 shows a typical microporosity shrinkage defect forming a network inside a LGI casting.

Figure 24 – Typical microporosity shrinkage inside a LGI casting. [41]

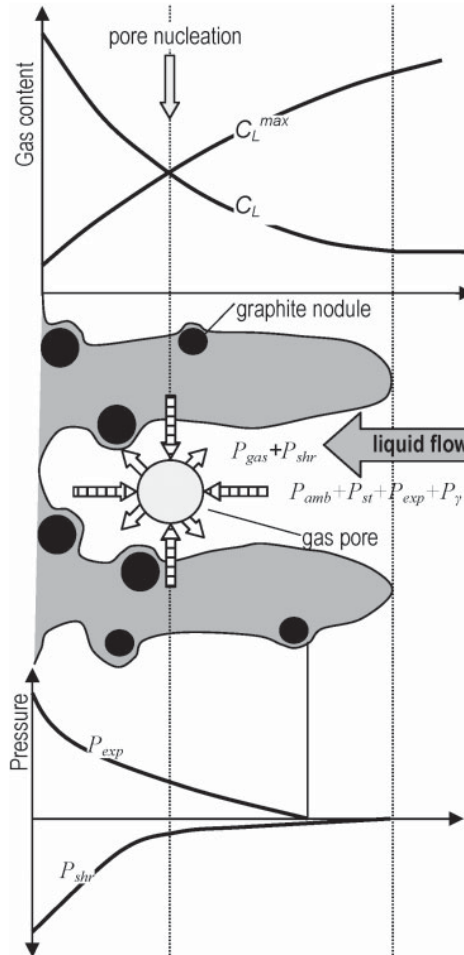


Source: ELMQUIST 2009

During the transformation from liquid to solid, most metals passes through a volumetric shrinkage from 3 to 10%, with 5 to 8% being a typical value for most cast alloys, then the melt starts to become more viscous, what turns the feeding of isolated voids harder, the chance to form shrinkage porosity inside the casting increases. [40]

Microporosity formation in the last to freeze areas can be better understood using the diagram in figure 25. It shows the pressure and gas content along the mushy zone of a SGI. [34]

Figure 25: Pressure and gas content at a SGI mushy zone.



Source: STEFANESCU 2005.

Recent models for microporosity formation assumes that it starts by the precipitation of a pore in the mushy zone after the dendrite coherency, where it is trapped in the dendritic network and is therefore, hard to feed with liquid metal. For nucleation and growth of a porosity to occur, the pressure of the gas must be higher than the sum of the local pressures in the mushy zone. [34]

$$P_G > P_{mush} + P_\gamma$$

Where

$$P_{mush} = P_{appl} + P_{st} + P_{exp} - P_{shr}$$

Where P_{appl} is the pressure over the mold, such as the atmospheric pressure, P_{st} is the metallostatic pressure, P_{exp} is the expansion pressure originated by phase transformation and P_{shr} is a negative pressure from the resistance to shrinkage induced flow through the solid dendritic network, rearranging the equation gives

$$P_G + P_{shr} > P_{appl} + P_{st} + P_{exp} + P_\gamma$$

Which means that gas and shrinkage pressures are the driving force for pore formation. Without the gas pressure, the shrinkage pressure must exceed the shear stress of the liquid in order to nucleate a vacuum pore. [34]

According to the diagram the gas pore can nucleate when the content of the gas in the liquid C_L exceeds the maximum solubility of the gas in the liquid C_L^{max} , figure 21.

The growth of the pore only occurs if the pore is stable; this stability is controlled by the surface pressure energy over the gas pore, defined by

$$P_\gamma = 2\gamma_{LG}/r$$

Where γ_{LG} is the gas-liquid interface energy and r is the pore radius. This equation suggests that the nucleation starts heterogeneously since the formation radius of a pore formed homogeneously would be too small, which would result in a high surface pressure energy. [34]

In ductile iron, the term P_{exp} comes from the graphite formation and if it is equal or superior to the shrinkage pressure, it can avoid microporosity completely. This would require a rigid mold, which is a hard condition to achieve in practice. [34]

Segregation of carbide stabilizing elements, to the last to freeze areas can also affect shrinkage formation, since carbides have a high density, the term P_{exp} is smaller and it would be easier to form microporosity. Some authors defend the use of special inoculants for SGI, that would cause a graphite formation in the last phase of solidification instead of carbide formation and generate graphite expansion by increasing P_{exp} and therefore, reducing shrinkage porosity formation. [42]

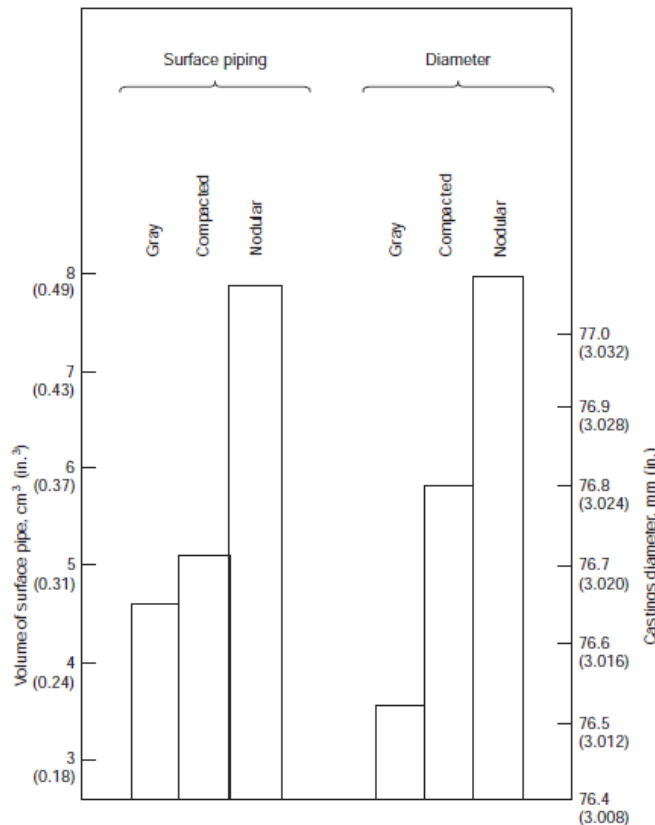
Magnesium is a powerful carbide-promoting element, when there is an overtreatment with this element during nodularization, it can segregate to last to freeze

areas and help to promote shrinkage porosity formation not only in SGI but also in CGI production. Cerium is even more powerful carbide promoting element than magnesium, which means that the tendency to increase nodularity when this element is used as a nodularizing agent is even bigger than magnesium. [8]

Vazehrad [2014] studied the influence of several parameters of CGI production on shrinkage formation, such as nodularity, eutectic cell size and distribution and N and H content in the metal. The results have shown that CGI has an increased tendency to form shrinkage porosity defects when the nodularity is increased, while the decrease in eutectic cell size could promote the formation the same defect. The amount of gases such as nitrogen and hydrogen can become an issue when their level grows beyond the solubility limits. [31]

Studies conducted by Sergeant [1978] have shown that CGI have shrinkage characteristics between those of SGI and LGI, figure 26. This means that, to obtain sound casting using CGI, the mold should have more rigid walls than for LGI and the gating and rising system should be similar to those used for SGI production. [43]

Figure 26: Comparison of shrinkage behavior in grey, compacted and ductile iron castings in green sand molds.



Source: SERGEANT 1978

The main problem with shrinkage porosity is that it has a strong impact on casting reliability, since micro-porosity shrinkage can interconnect internally and lead to leakage in castings parts such as cylinder blocks, e.g. refrigeration chambers connecting to fuel channels. [41] Porosity also can form close to the casting surface, where the machining process can reveal it, causing the scrap of the part due to isolation problems and negative impact over mechanical properties.

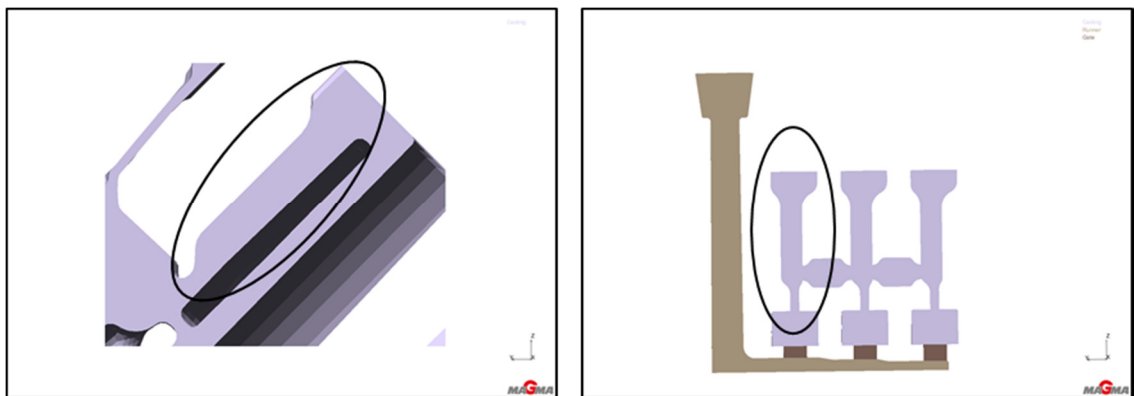
3 EXPERIMENTAL PROCEDURE

The aim of this section is to present the materials and methods used in order to achieve the work goals. In order to study shrinkage porosity formation, it is essential to use a specimen sensible to the variables under study; this section presents this specimen and an experimental matrix that shows the different variables combinations used in the study. The end of the section describes the characterization methods used in the work.

3.1 SPECIMEN GEOMETRY AND EXPERIMENTAL ARRANGEMENT

The specimen copies a typical geometry of a particularly challenging region of a cylinder block, with a thin section feeding a thick section. The region between the cylinders and water galleries and close to an oil channel usually presents this geometry. Figure 27 shows a typical profile of the region and the first geometry of the specimen used in this study.

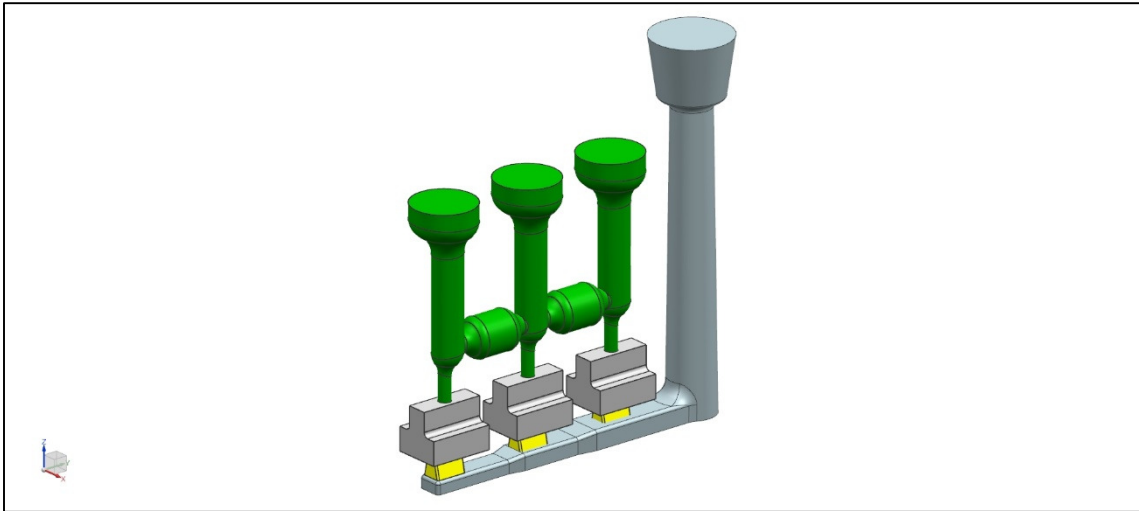
Figure 27 - Cylinder block region profile and the specimen geometry.



Source: Author 2016.

Figure 28 shows a 3D view of the first geometry tested in order to obtain a specimen that could simulate shrinkage porosity occurrence.

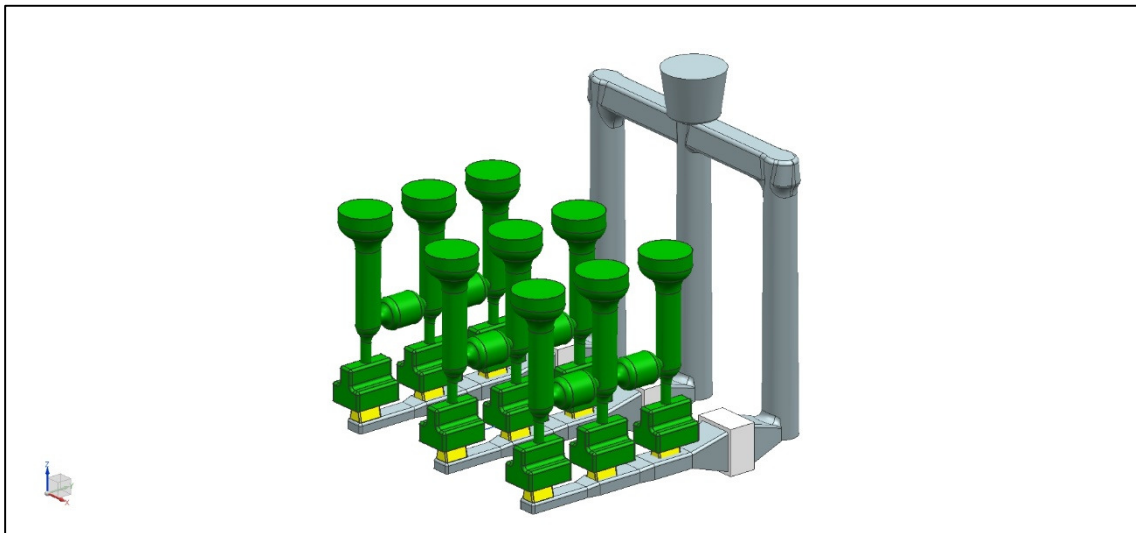
Figure 28: First specimen design used to simulate shrinkage defect.



Source: Author 2016

Figure 29 shows an arrangement of three samples per mold made in order to cast more samples for each experiment.

Figure 29: Specimen arrangement.

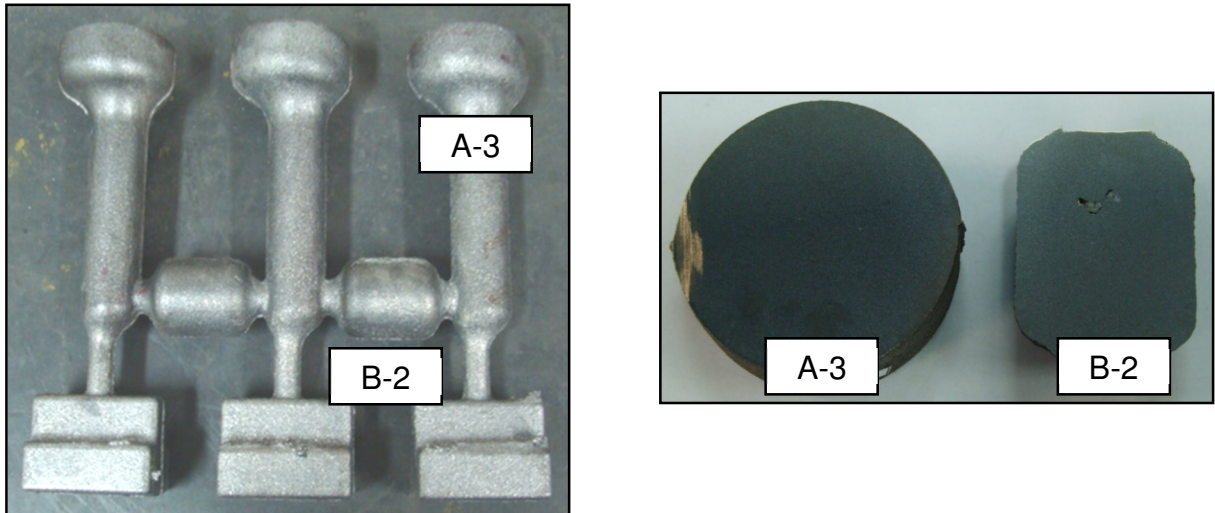


Source: Author 2016

Using this design, the first run had the aim to test two different magnesium contents to check the specimen sensibility to the defect. Due to problems during the run, it was not possible to use two different magnesium contents, only one, of about 0,012%, for the two arrangements (6 samples).

After shake out, the specimens were submitted to x-ray and ultrasound testing to look for defects and, even with this low Mg, two samples presented defects in different regions, figure 30 shows the regions with the defects.

Figure 30: Cast specimen and regions with defect.



Source: Author 2016

The defect identified at region A-3 was only detected using ultrasound testing and figure 31 shows its microstructure. This defect was found in one of the regions that is expected to have shrinkage and in only one specimen of the 6 that were casted. It has the aspect of lustrous carbon.

Figure 31: Region A-3 defect microstructure.



Source: Author 2016

The other defect (Region B-2) was in a different specimen than the first, figure 32 shows the defect. It was also in only one specimen from the six that were casted. The nodularity of regions A-3 and B-2 is 16 and 24, respectively.

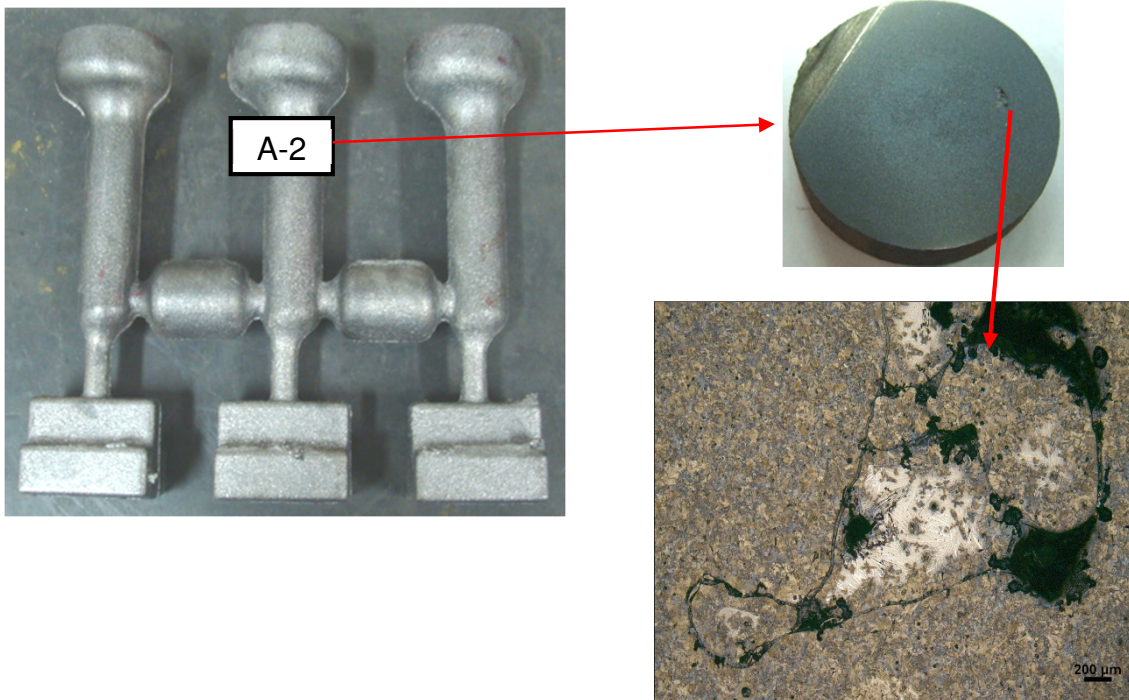
Figure 32: Region B-2 defect microstructure.



Source: Author 2016

Since the two levels of Mg were not achieved in the first trial, a second trial was planned using the same geometry, this time, obtaining the Mg amounts of 0.016% and 0.023%. The geometry presented defect in only one region for the high Mg content specimen. Figure 33 shows the region and the defect, the nodularity of this sample is 17%.

Figure 33: Second trial specimen with high Mg content, region A-2 defect.



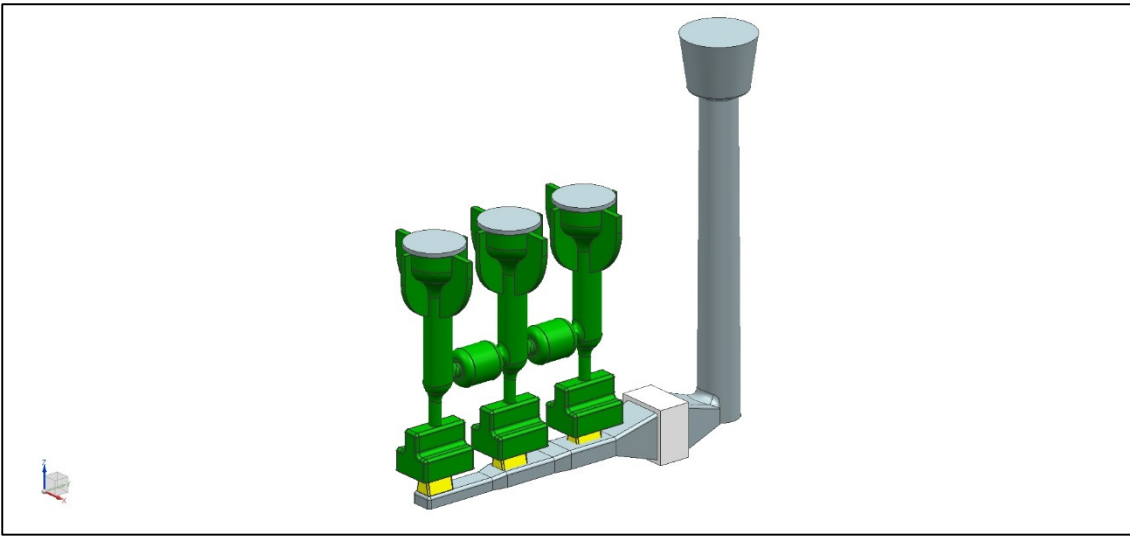
Source: Author 2016

This defect is very similar to the one found in the previous test in region A-3, it also have the aspect of lustrous carbon.

It was observed in the previous specimen what seemed to be a small surface contraction in the top of the specimens. Therefore, for the third trial, a chill, in the form of a disc, was added at the top of the sample.

Another change in the geometry was based on the cylinder block geometry, which has some thin ribs attached to it, so the specimen for the new trial was modified to add four thin ribs around the top region of the specimen. Figure 34 shows the new specimen geometry.

Figure 34 - Specimen Design for the third trial.

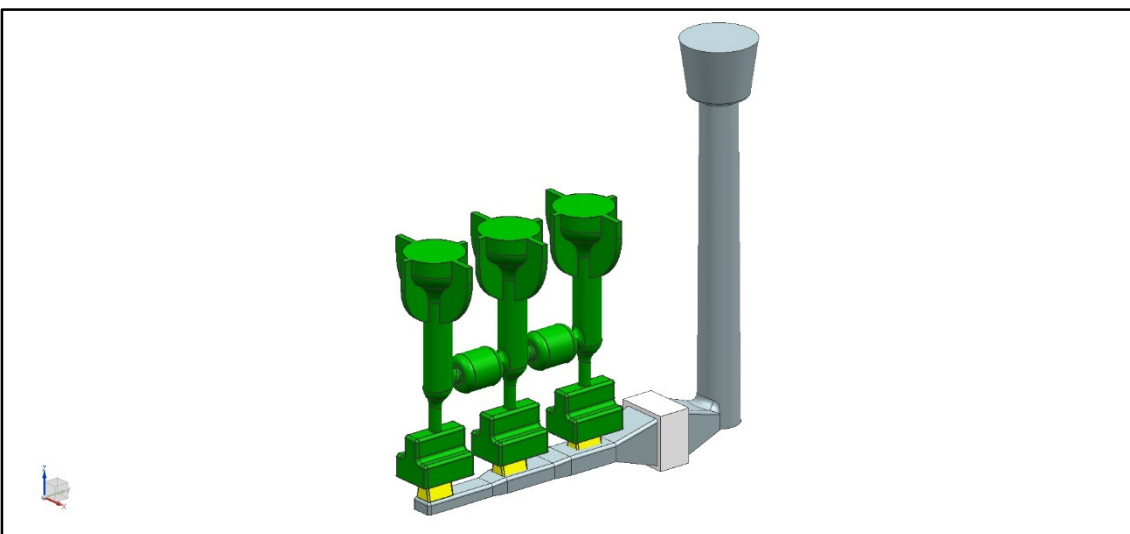


Source: Author 2016

The third trial used the same parameters as the second, with medium and high Mg content, and an assembly of three samples per mold, changing only the previously mentioned aspects. The test was inconclusive because the metal was not able to fill the cavity. Probably the chills blocked the gas exit, creating too much pressure over the metal surface and preventing it from filling the cavity.

Based on this consideration the fourth trial used the same geometry as the third one but without the chills. Figure 35 shows the design used for the fourth trial.

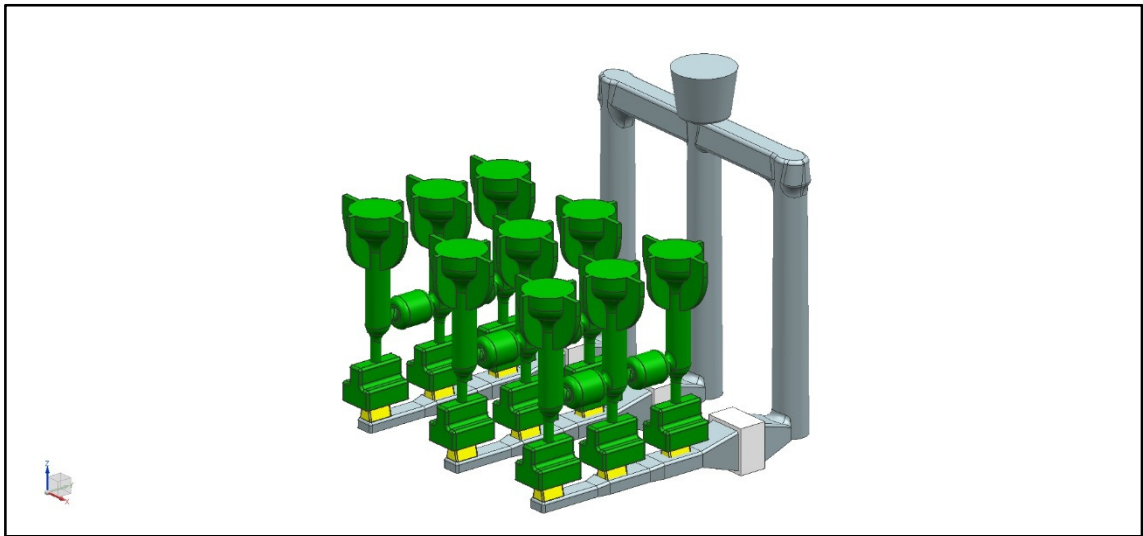
Figure 35 - Specimen design for the fourth trial.



Source: Author 2016

For the fourth trial four assemblies of specimens were made, two were casted with Mg content of 0.013% and two with 0.020%. It was also decided to use a graphite based coating on the cores in an attempt to prevent lustrous carbon formation. All the samples presented shrinkage porosity defects for this set, but with different sizes and characteristics for the two levels of Mg content. Therefore, this geometry was chosen to be used on the experiment. Figure 36 shows the experimental assembly.

Figure 36 – Experimental assembly.



Source: Author 2016

3.2 MATERIALS

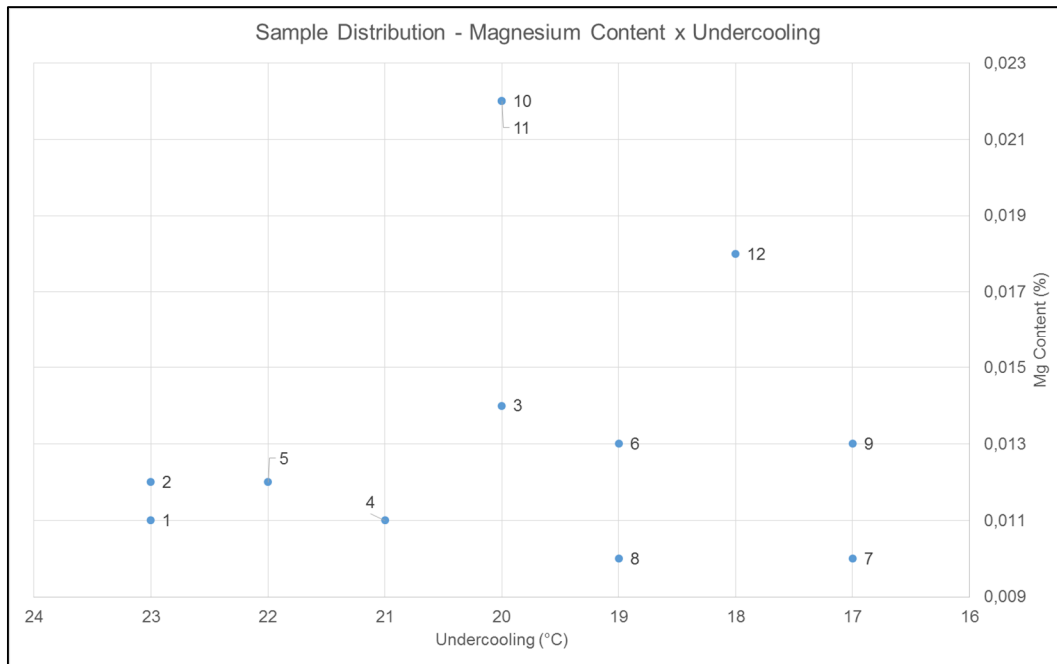
The casting alloy used in this experiment is based on a compacted graphite cast iron of hypereutectic composition.

The magnesium content and undercooling obtained during the experiment are displayed in the graphic shown by figure 37. The method used for magnesium content measurement is described in section 3.3. Undercooling was measured directly from the thermal analysis curve from SinterCast by subtracting the undercooling temperature from the stable eutectic temperature from the alloy composition of the samples.

Due to difficulties during pouring of the samples, conditions with low inoculation level, high undercooling, combined with high magnesium content, above 0.018%, were not achieved.

As stated in the specific objectives, section 1.2, the goal is to analyze the effect of these variables in the material solidification and, therefore, in the shrinkage porosity formation, from a level below the process lower limit to a level above the process higher limit.

Figure 37 - Sample distribution inside the experimental matrix.



Source: Author 2016

The specimens were poured using typical cold box process cores. The cores used for casting the specimen are manufactured using silica sand with the following parameters:

- Average grain fines number: 74
- AFS Clay: 0.09%
- Humidity: 0.1%
- Fines: 3.25%
-

Prior to the assembly of the experiment arrangement, the cores were coated using a graphite-alcohol based coating.

3.2.1 Nodularization treatment

SinterCast thermal analysis control process was used to control the magnesium and inoculant additions. This process uses a two steps addition of nodularizing elements, a first addition is made using Mg cored wire when the ladle arrives with the base metal, called the pre-treatment. A thermal analysis is performed and a second addition, called after treatment, is calculated based on the result of the first addition.

Then the metal was poured into the molds. The pouring temperature for the samples ranged from 1385 to 1390 °C.

3.3 CHEMICAL ANALYSIS

The analysis of the cast specimens was done using the foundry production equipment. The equipment is an optical emission spectrometry Model ARL 3460 METAL ANALYZER from ThermoFisher Scientific.

The samples were collected using a copper refrigerated chill, in disc formats, immediately after the pouring of the samples. Table 1 shows the magnesium content and carbon equivalent along with the undercooling obtained by the experiment.

Table 1: Magnesium content, undercooling and CE of the cast samples.

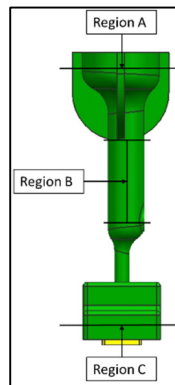
Sample Number	CE (%)	Mg (%)	Undercooling (°C)
1	4.42	0.011	23
2	4.51	0.012	23
3	4.45	0.014	20
4	4.45	0.011	21
5	4.45	0.012	22
6	4.45	0.013	19
7	4.47	0.010	17
8	4.45	0.010	20
9	4.45	0.013	18
10	4.49	0.022	20
11	4.49	0.022	20
12	4.47	0.018	19

Source: Author 2018.

3.4 MICROSTRUCTURAL CHARACTERIZATION

This section describes the methodology used for microstructure characterization, which divides into graphite analysis, color etching and eutectic cells analysis. Figure 38 shows the regions where the metallographic analysis were performed.

Figure 38: Regions used for microstructure evaluation.



Source: Author 2018.

3.4.1 Graphite Analysis

The sample examination regarding graphite morphology were performed according to ASTM E 3-11, ASTM E7-09, NBR6593 and NBR 8108:1983 standards. The optical microscope was an OLYMPUS BX41M-LED and Image pro-plus image analyzer, version 7.0.

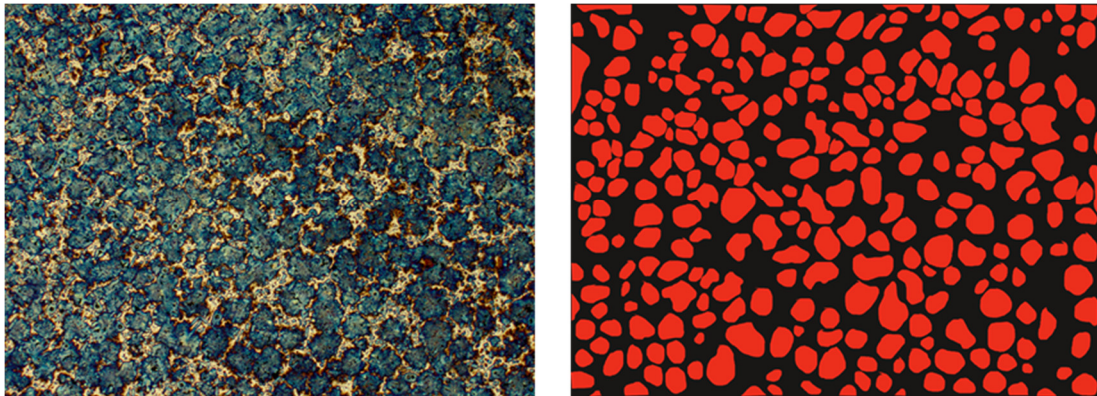
3.4.2 Color Etching

Color etching was performed using a picral acid based solution, with the following composition: 10 g picric acid, 10 g NaOH, 40 g KOH and 50ml distilled water, also known as Motz etchant. The solution is held in a temperature between 100°C and 110°C and the samples are submerged in the solution for a time between 3 and 5 minutes. [45]

3.4.3 Eutectic Cell Analysis

For the eutectic cell evaluation, four color-etched micrographs were made for each test condition using optical microscopy (Olympus GX71F) and transformed into a binary image, where eutectic cells were represented as red color objects; the program used for the transformation was Photoshop. Figure 39 shows an original color-etched micrograph and its binary transformation. The binary images were used for mean diameter and area fraction measurements; the region where the measurements were carried out was the region in the middle radius since it represents most of the sample.

Figure 39 - Color Etched micrograph and its binary form used for eutectic cell mean diameter and area fraction measurements.



Source: Author 2018.

For the mean diameter measurements, the eutectic cells located in the edge of the image were not considered, since it is not possible to know their total dimensions.

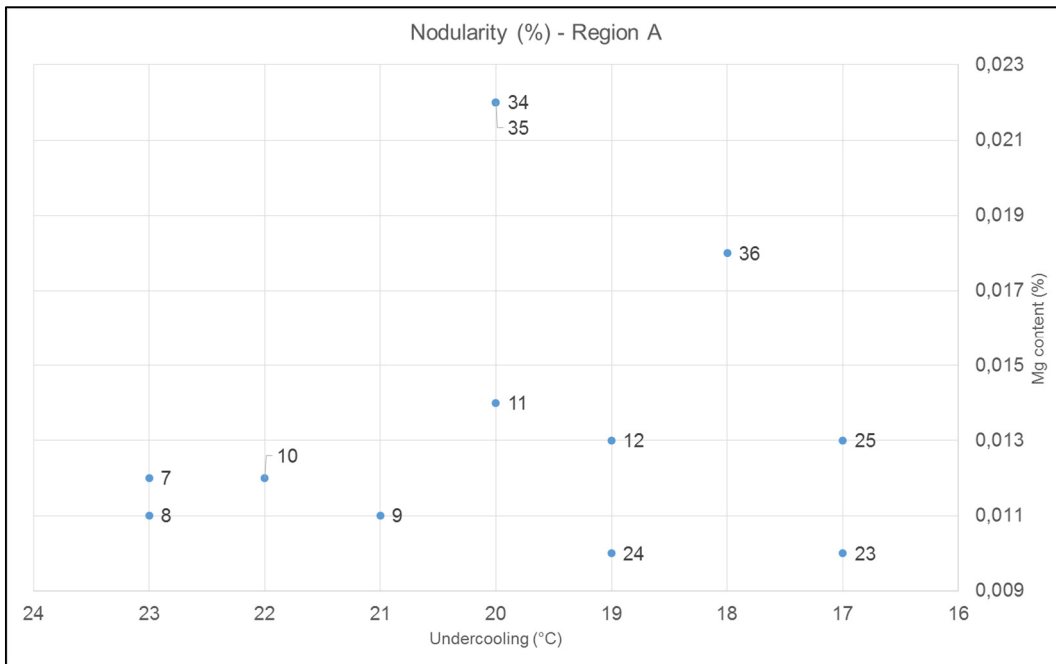
4 RESULTS AND DISCUSSION

This chapter presents and discusses the main results obtained through the experiment. The chapter divides into the following sections: influence of the studied parameters over nodularity, colour etching investigation, influence of the studied parameters over compacted graphite eutectic cell colony size and distribution, porosity analysis and influence of the studied parameters over porosity occurrence.

4.1 INFLUENCE OF THE STUDIED PARAMETERS OVER NODULARITY

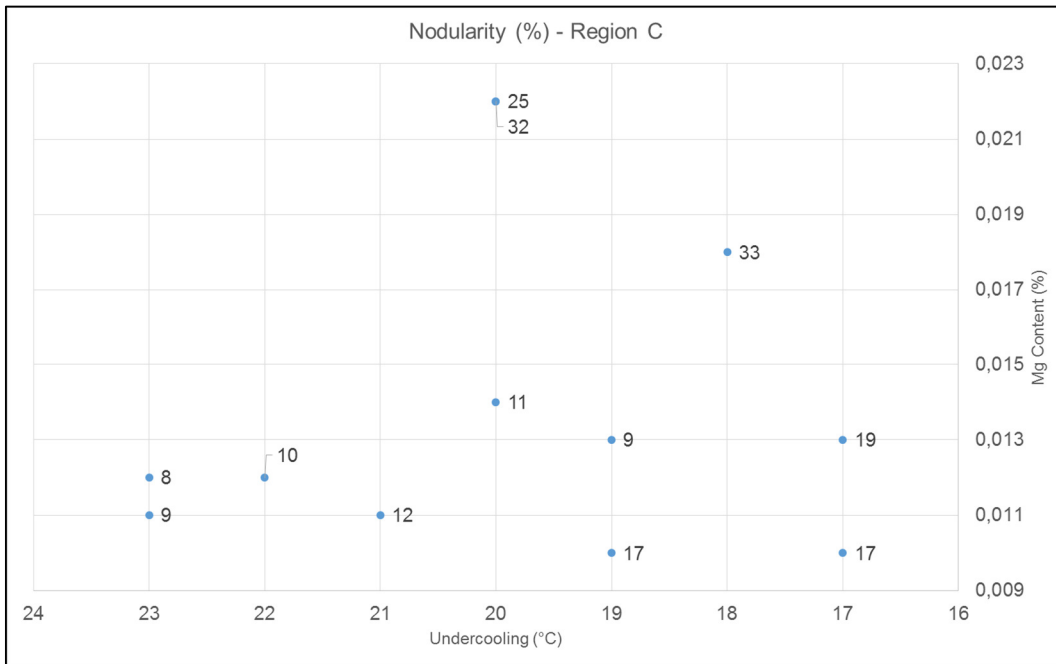
The diagrams shown by figures 40 and 41 summarize the effect of both magnesium and inoculant addition over nodularity in regions A and C. Both diagrams show a significant increase in nodularity for the smallest undercooling, 17, 18 and 19°C, and for the highest magnesium content, of 0.018 and 0.022%. The highest results being measured for magnesium content above 0,018% and undercoolings of 18 and 20°C. For magnesium content below 0.018%, the nodularity increased only for high levels of inoculation, with undercoolings of 17, 18 and 19°C.

Figure 40: Variation in nodularity according to the variation in undercooling and magnesium content. Region A.



Source: Author 2018

Figure 41: Variation in nodularity according to the variation in undercooling and magnesium content. Region C.



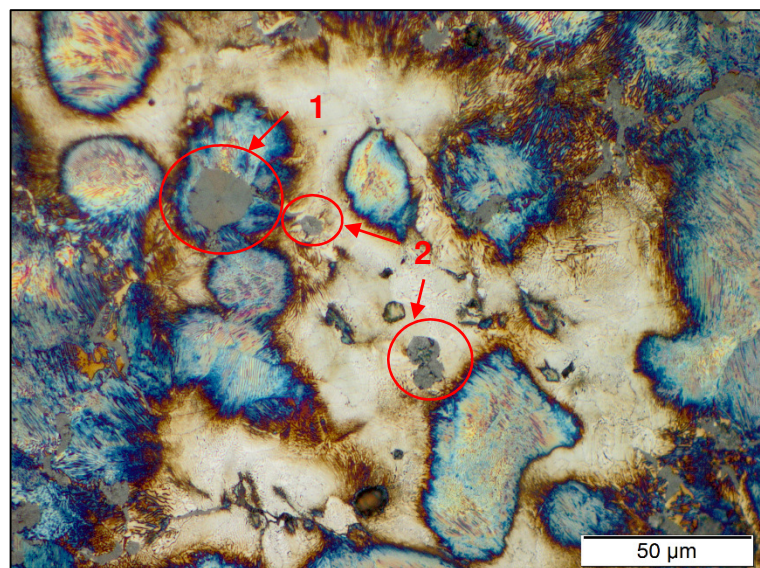
Source: Author 2018

There is no significant changes in nodularity when undercooling is reduced from 23°C, small levels of inoculation, to 21 or 20°C, medium levels of inoculation, this indicates that, for the two regions under analysis, there is a determined inoculation level that starts influencing the nodularity; below this level the variations have no impact over nodularity.

In both regions, A and C, the increase in nodularity for the cases described in this section is achieved by an increase in nodular graphite eutectic cells which seems to be solidifying segregated from compacted graphite eutectic cells, as also observed by Domeij, for holding times above 30 minutes with nodularity around 40%. [46] For all samples, the nodules were rarely seen inside the compacted graphite eutectic, but in their periphery, both as an early solidified nodule, surrounded by silicon rich area, or as a late solidified nodule, surrounded by a low silicon area, as described by other authors. [28] [3] Both types of nodules are visible in figure 42.

There is a tendency for lower nodularity in region C when compared to region A, this is probably caused by a lower cooling rate of Region C, reducing the nodularity in this region.

Figure 42: Color etched sample showing graphite nodules located between compacted graphite eutectic cells in two different conditions. 1 - larger nodule, surrounded by silicon rich area and 2 - smaller nodule surrounded by a low silicon area.



Source: Author 2018.

4.2 COLOUR ETCHING INVESTIGATION

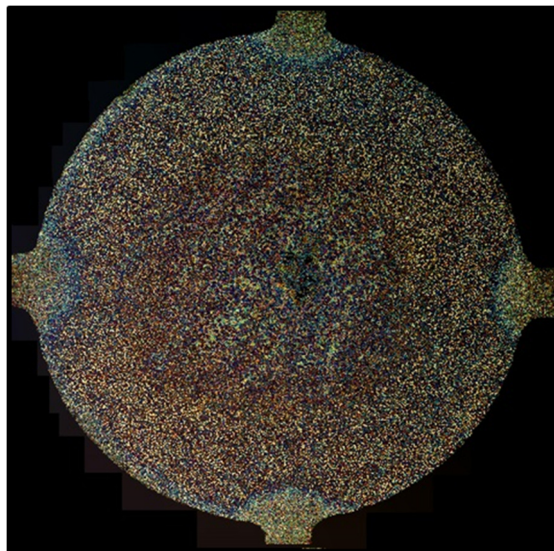
The colour etching technique reveals the final solidification microstructure of the samples; the analysis was performed in three distinct regions according to chapter 3, region A, region B and region C. The analysis in regions A and C reveals the microstructure according to figure 38, the microstructure found in these two regions are very similar and the discussion made for region A is valid for region C as well.

The analysis in region B reveals the microstructure in a parallel cut, according to figure 30, since the objective was to identify how the variation in magnesium content and inoculation level affects the microstructure of the region connecting regions A and C.

4.2.1 Region A

Figure 43 shows an example of an examined section in region A using color etching and optical microscopy.

Figure 43: Typical microstructure revealed by color etching on region A.

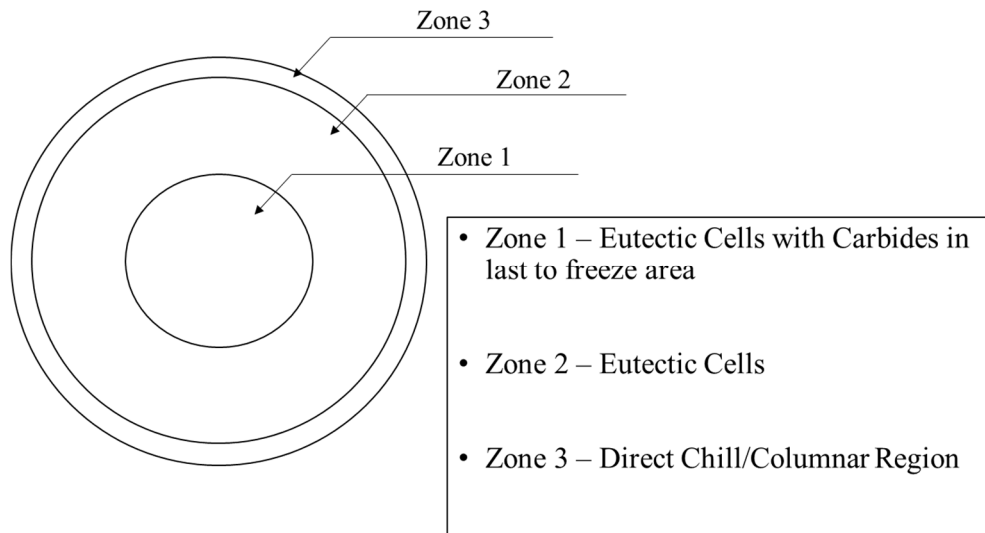


Source: Author 2018

There are three distinct zones in every sample examined, according to the diagram in figure 44, each of these zones have different microstructures, figure 45. Zone 1, has eutectic cells surrounded by carbides in last to freeze areas, Zone 2 has eutectic cells and last to freeze areas and Zone 3 has columnar microstructure that

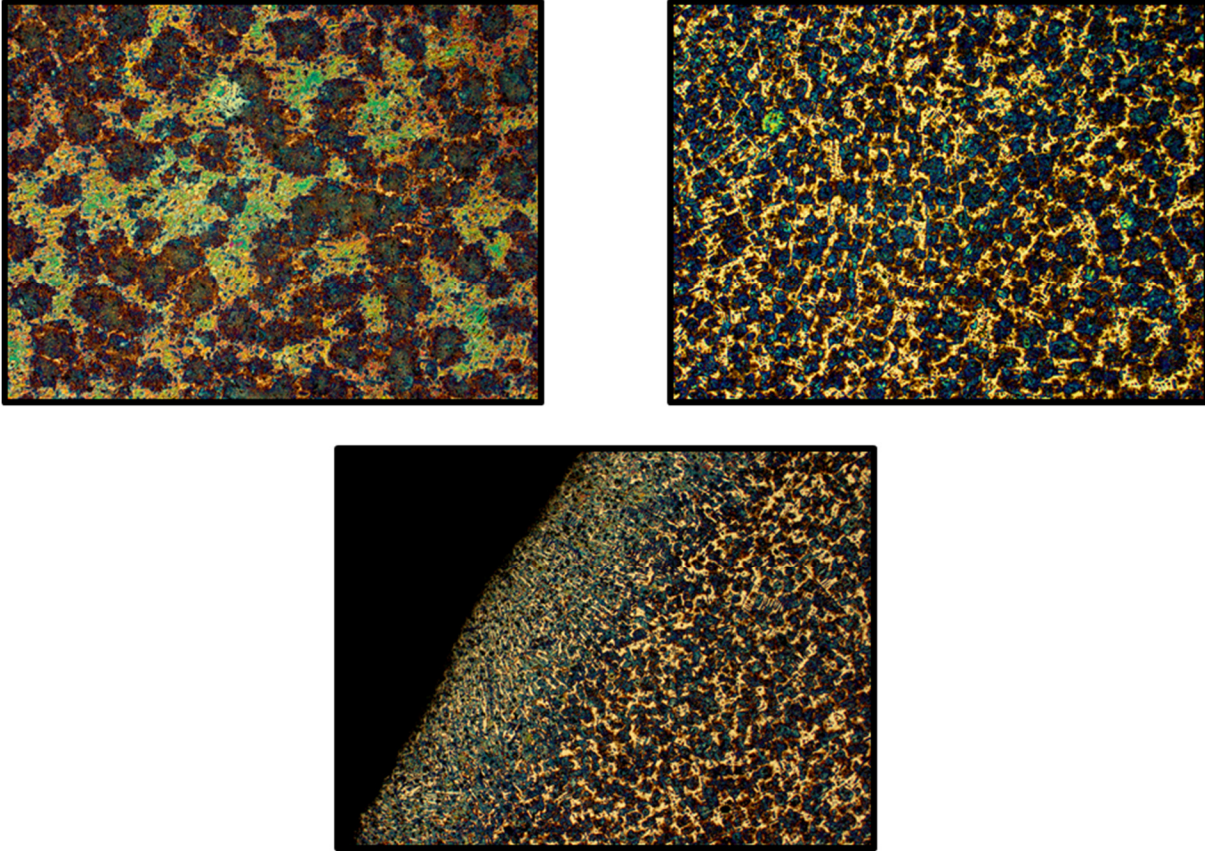
varied between columnar dendrites to direct chill carbides depending on the experiment condition.

Figure 44: Diagram of the section different sites, based on the differences in microstructure.



Source: Author 2018.

Figure 45: Details of the microstructure in the three different sites. (a) Zone 1 - Eutectic Cells with Carbides in last to freeze area (b) Zone 2 - Eutectic Cells (c) Zone 3 - Direct Chill/Columnar Region. Amplification: 25x.



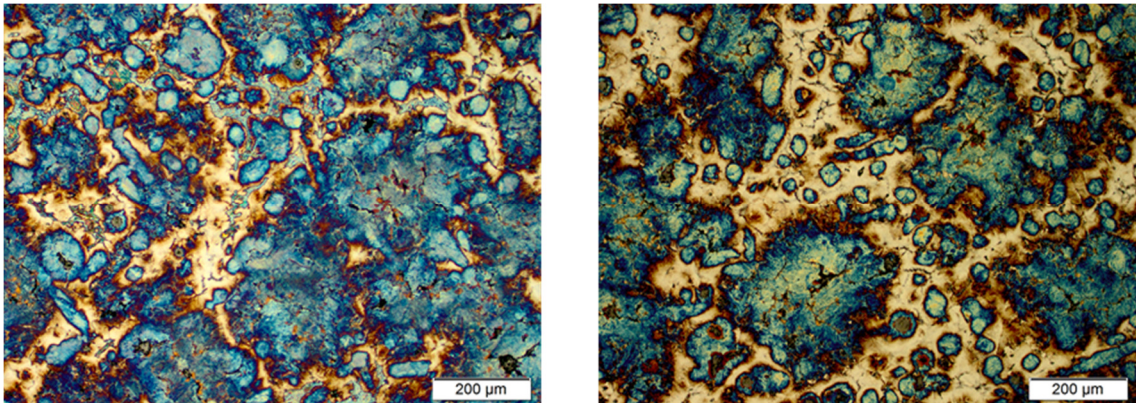
Source: Author 2018

Characterization of zone 1 reveals a large amount of intercellular space and the presence of inverse chill carbides between the eutectic cells. The samples with less inverse chill formation seem to have smaller shrinkage porosities, which are located in the same regions where the inverse chill are, between the eutectic cells, in the last to freeze areas; they also have higher amounts of spheroidal graphites in the last to freeze areas.

The substitution of carbides by spheroidal graphites, with their expansion effect, which in last to freeze areas, goes directly to the liquid due to the absence of the enveloping austenite, could be the reason why these samples have smaller shrinkage or no shrinkage at all.

Figure 46 shows microstructures containing inverse chill carbides and nodules in last to freeze areas in zone 1.

Figure 46 - Inverse chill carbides (left) and spheroidal graphites (right) in last to freeze areas in zone 1. Amplification 50x.



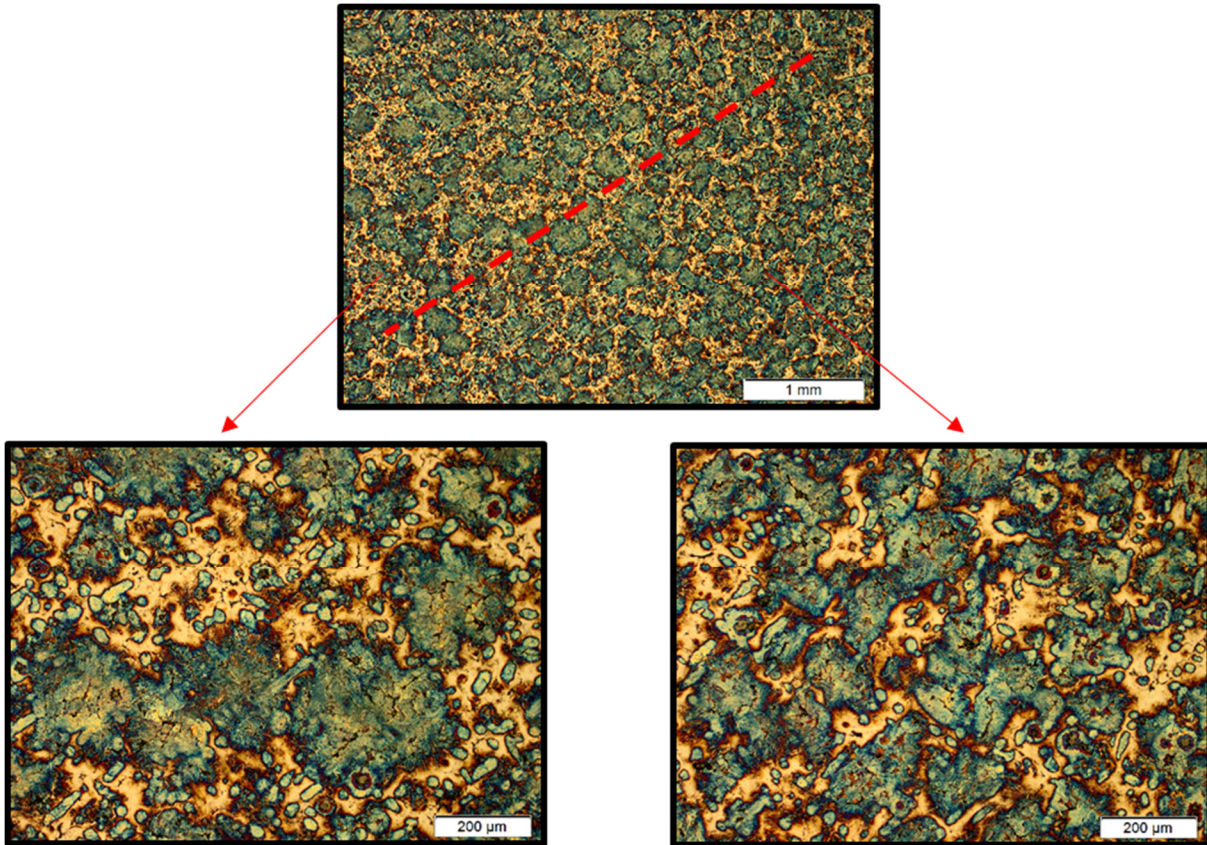
Source: Author 2018.

The amount of inverse chill carbides observed in this in zone 1 of this region did not present any clear relation with inoculation levels or magnesium content variations used in the experiment.

A qualitative examination of zone 2 shows that the eutectic cell structure is more homogeneous in the region close to zone 3 (zone 2-b), where the cells are smaller and have less intercellular space, while in the region close to zone 1 (zone 2-a) the cells are larger and have more intercellular space, figure 47 shows this feature.

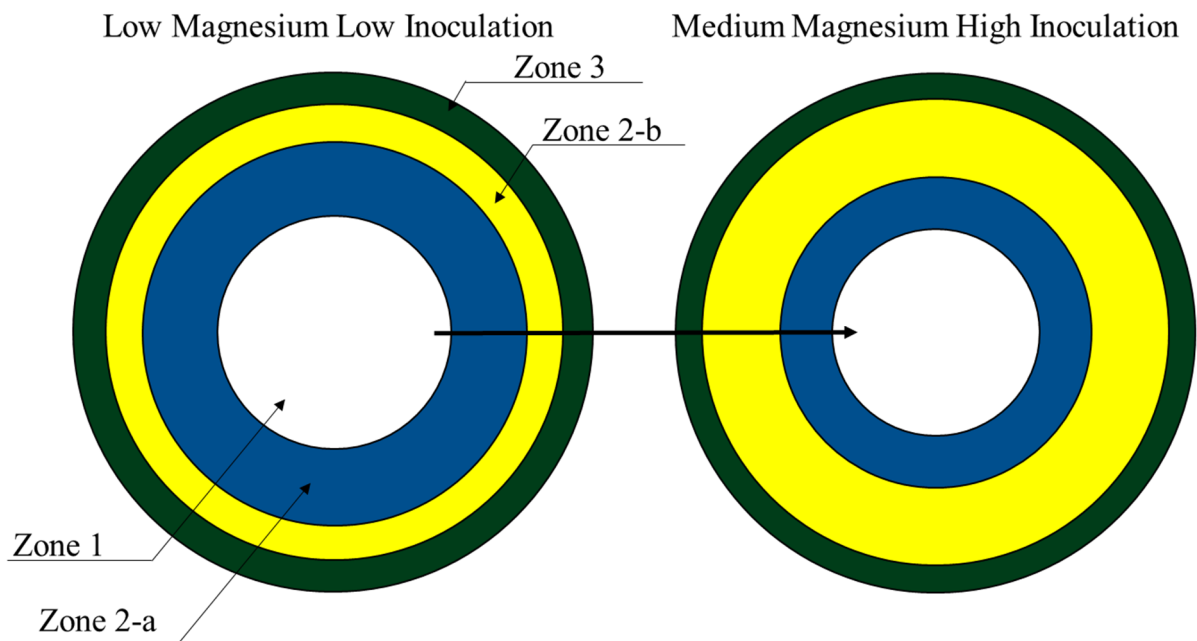
The proportion between zone 2-a and zone 2-b change as the experimental conditions change. By increasing the amount of inoculation from low to high level, the microstructure in zone 2 becomes more homogeneous, as in zone 2-b, the eutectic cells are smaller and more evenly distributed through the section as illustrated by the diagram on figure 48.

Figure 47: Further characterization of the samples different sections, on the left side the eutectic cells are larger and have more intercellular space and on the right side the eutectic cells are smaller and have less intercellular space between them.



Source: Author 2018.

Figure 48: Effect of increasing levels of magnesium and inoculation over zone 2, there is an increase in the smaller eutectic cells with less intercellular space between them, at the same time that the larger eutectic cells with more intercellular space between them decreases.



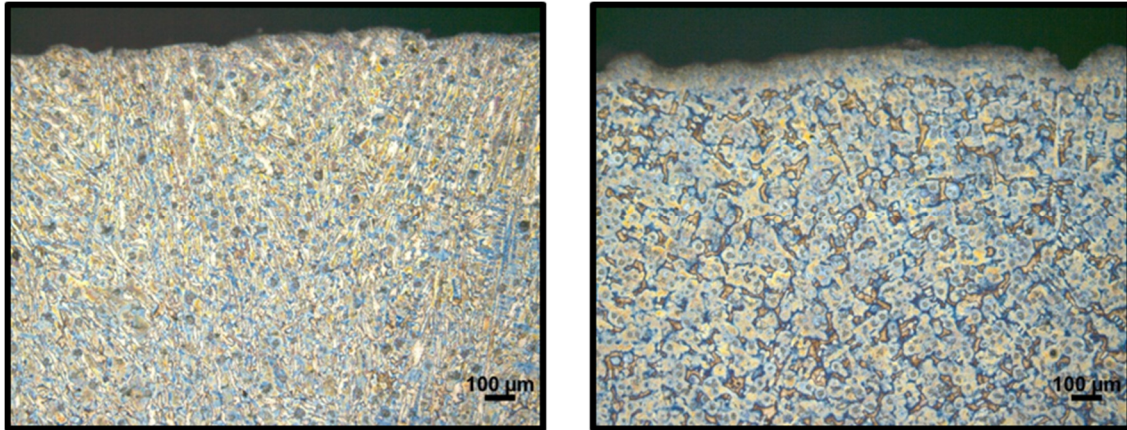
Source: Author 2018.

4.2.2 Region B

The evaluation in region B shows how the microstructure between regions A and C varies with varying amounts of magnesium and inoculation to help understand the different shrinkage porosity types that formed in these two regions. Region B also has two different zones that resembles zones 2 and 3 from region A. Zone 2, in the center of the samples and zone 3 close to its surface.

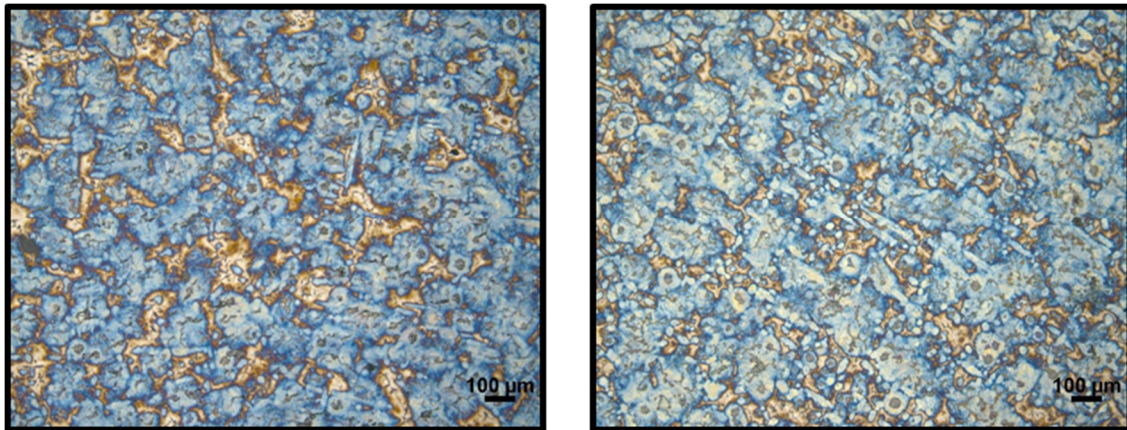
Figure 49 shows how the microstructure in the surface of the sample changes by decreasing the undercooling from 23 to 17°C, minimum inoculation level to maximum, and keeping magnesium content in the lower level, varying from 0.011 to 0.010%. Figure 50 shows how the microstructure in the centreline of the sample changes in the same samples shown in figure 49.

Figure 49: Microstructure in the surface of Region B. White eutectic growing from the surface (Left) and fine grey eutectic with high nodularity and columnar dendrites growing from the surface (Right)



Source: Author.

Figure 50: Microstructure in the centreline of Region B. Grey eutectic with last to freeze area between them and low nodularity (Left) and fine grey eutectic with high nodularity, last to freeze areas more evenly distributed and more presence of columnar dendrites (Right).



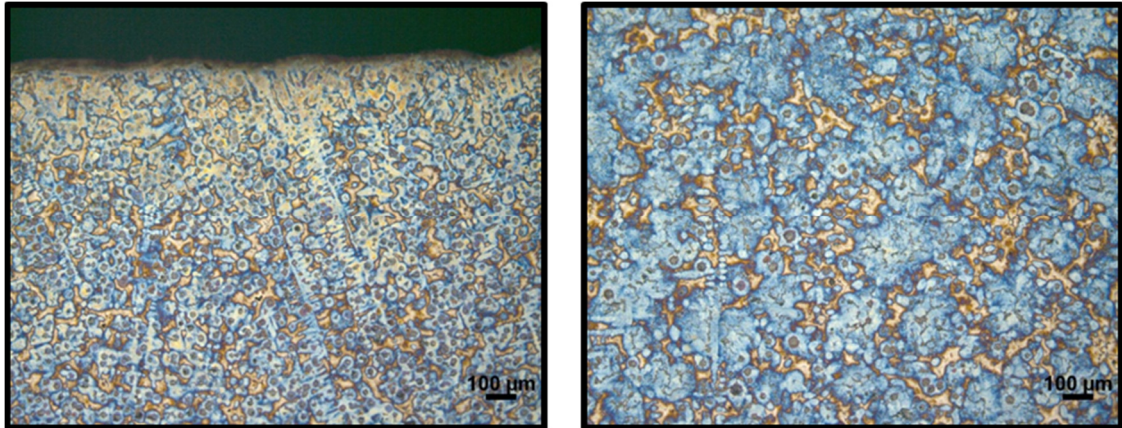
Source: Author.

The increase in inoculant level prevents the formation of the white eutectic in the surface and turns the structure in the centre of the sample more refined and with the last to freeze areas more evenly distributed along the section. Other perceivable effects are the increase in columnar dendrites and number of nodules visible in the section.

The increase in magnesium to the maximum content, of 0.022%, with an undercooling of 20 °C increases the nodularity to higher level and keeps the refinement

of the structure in what seems to be an intermediary level between the level of refinement of the undercoolings of 23 and 17°C. Figure 51 shows the microstructure for the surface and centre of the samples with these set of parameters.

Figure 51: Microstructure in the surface (left) and centre (right) of region B from the sample with magnesium content of 0.023% and undercooling of 13°C.



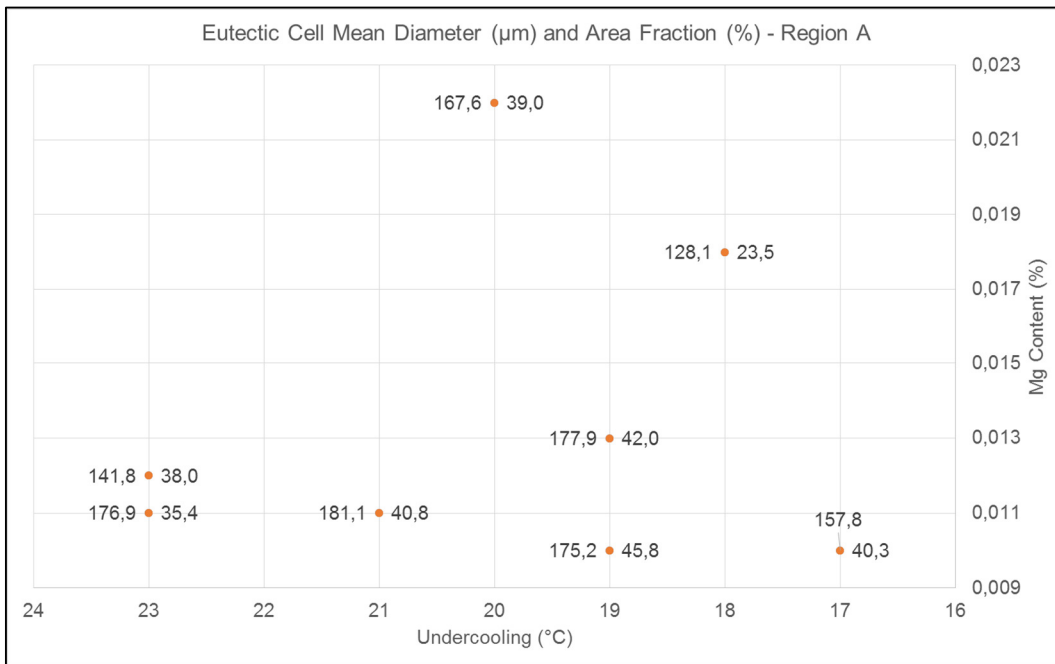
Source: Author.

4.3 INFLUENCE OF THE STUDIED PARAMETERS OVER EUTECTIC CELL SIZE AND DISTRIBUTION

The graphic in figure 52 shows the influence of the studied parameters over the mean area fraction of CGI eutectic cells and the mean diameter of CGI eutectic cells in region A. Although both samples with magnesium content above 0.018% have similar nodularity, there is an important difference, which is only identified by colour etching, which is the amount of last to freeze area between the eutectic cells.

The eutectic cell in the sample with 0.022% magnesium are larger than the ones in the samples with 0.018% magnesium and the space between eutectic cells is almost inexistent. These facts were also detected by the measurement of eutectic area fraction in the samples that is significant smaller for the samples with 0.018% magnesium and 18°C of undercooling.

Figure 52: Eutectic cell mean diameter (μm), values to the left of the dots, and area fraction (%), values to the right of the dots. Region A.

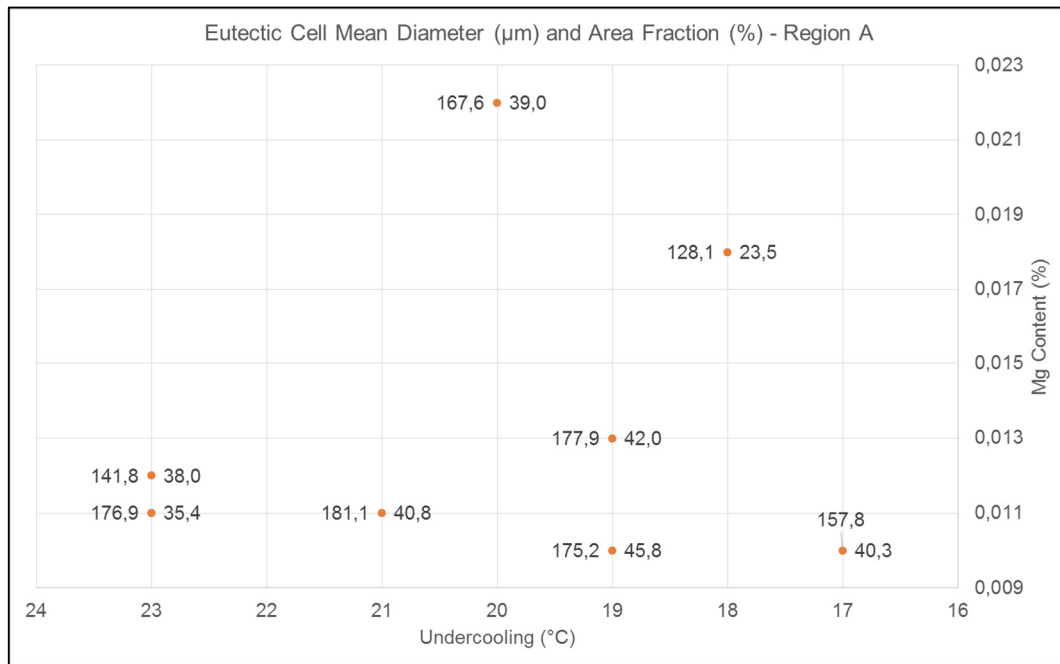


Source: Author 2018.

The data for the other samples does not seem to present any significant variation that can be explained by the analysis made during this work.

The graphic in figure 53 shows the influence of the studied parameters over the mean area fraction and the mean diameter of eutectic cells for region C. The data follows a similar trend for region C than it had for region A, with the samples with 0.022% of magnesium and 20°C of undercooling having larger eutectic cells and less last freeze areas between them compared to the samples with 0.018% of magnesium and 18°C of undercooling.

Figure 53: Eutectic cell mean diameter (μm), values to the left of the dots, and area fraction (%), values to the right of the dots. Region C.



Source: Author 2018.

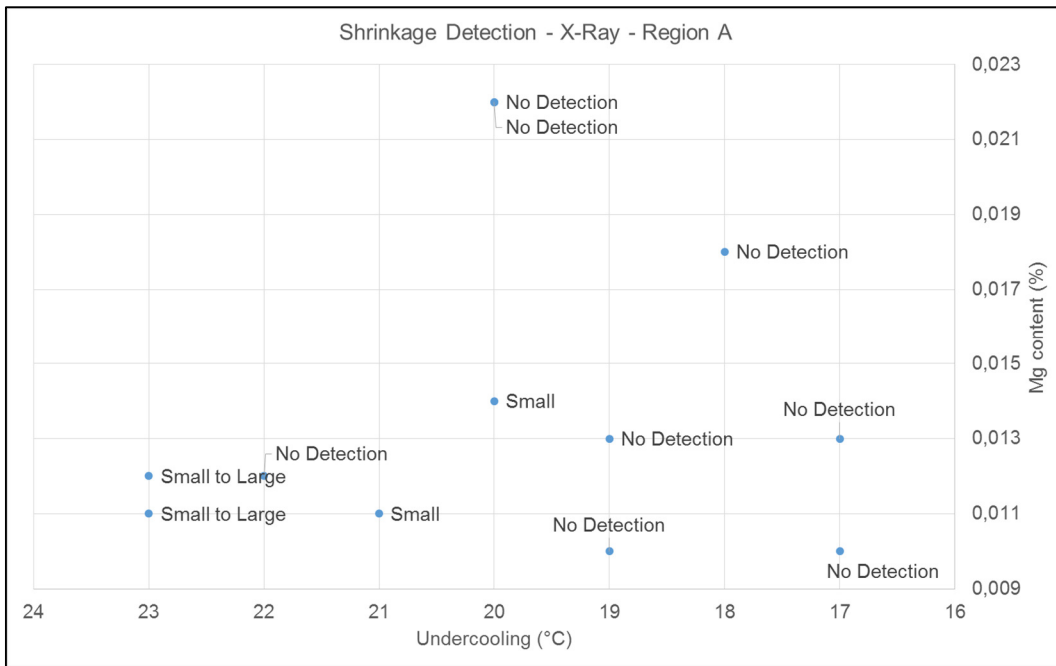
4.4 POROSITY

This section presents the identification and classification of the porosities found in the samples regarding their size and distribution and how the parameters under study relates to the porosity formation.

4.4.1 X-Ray Inspection

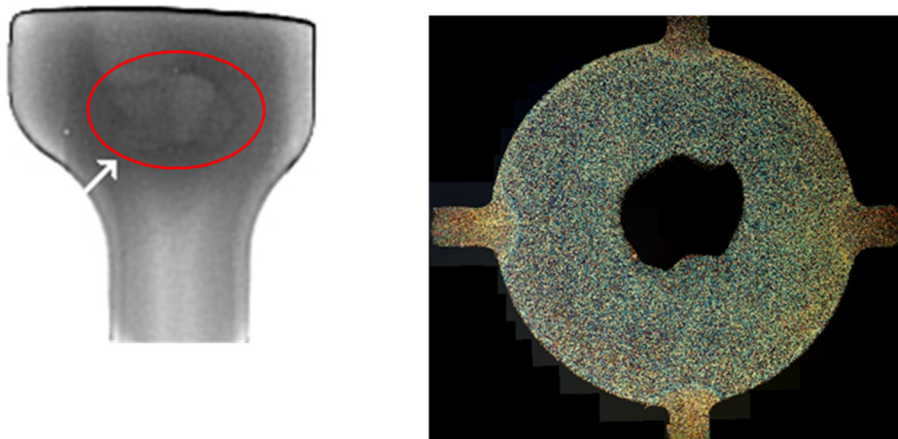
The industrial X-Ray detector identifies which samples presents porosities and their size and distribution in the samples. Figure 54 shows the porosity distribution among the samples while figures 55 to 57 shows samples of three different sizes of porosity identified in region A during the experiment, along with colour-etched metallography of the section.

Figure 54: Diagram showing the X-Ray testing results for each experimental condition - Region A.



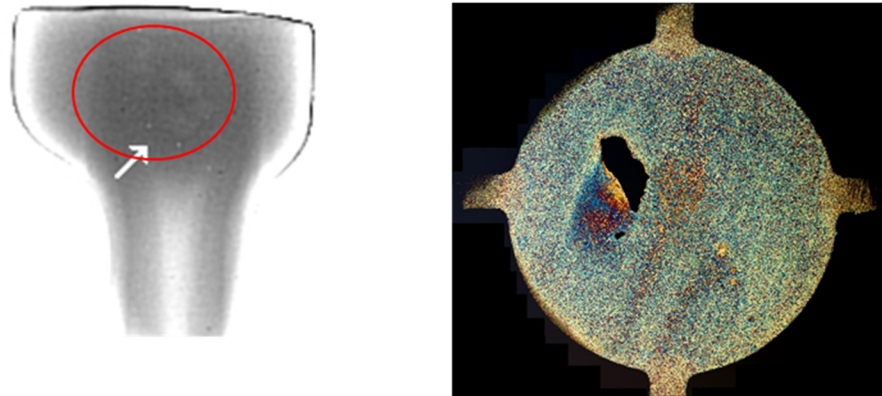
Source: Author 2018

Figure 55: Large size porosity in the Specimen. (Left) X-Ray image (Right) Colour-Etched section of the same sample.



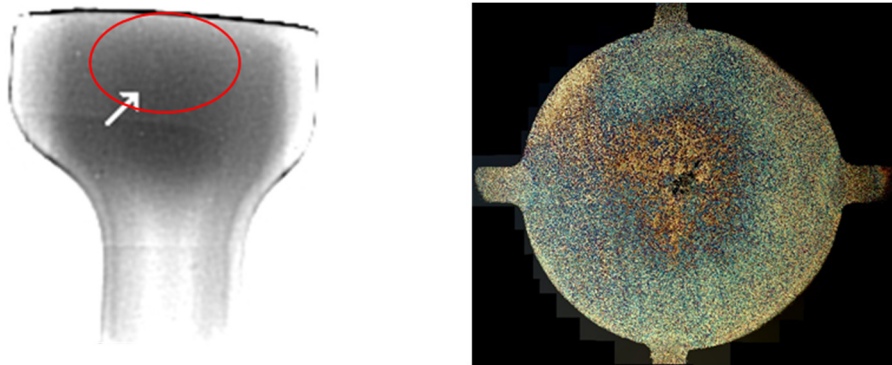
Source: Author 2018

Figure 56: Medium size porosity in the Specimen. (Left) X-Ray image (Right) Colour-Etched section of the same sample.



Source: Author 2018

Figure 57: Small size porosity in the Specimen. (Left) X-Ray image (Right) Colour-Etched section of the same sample.



Source: Author 2018

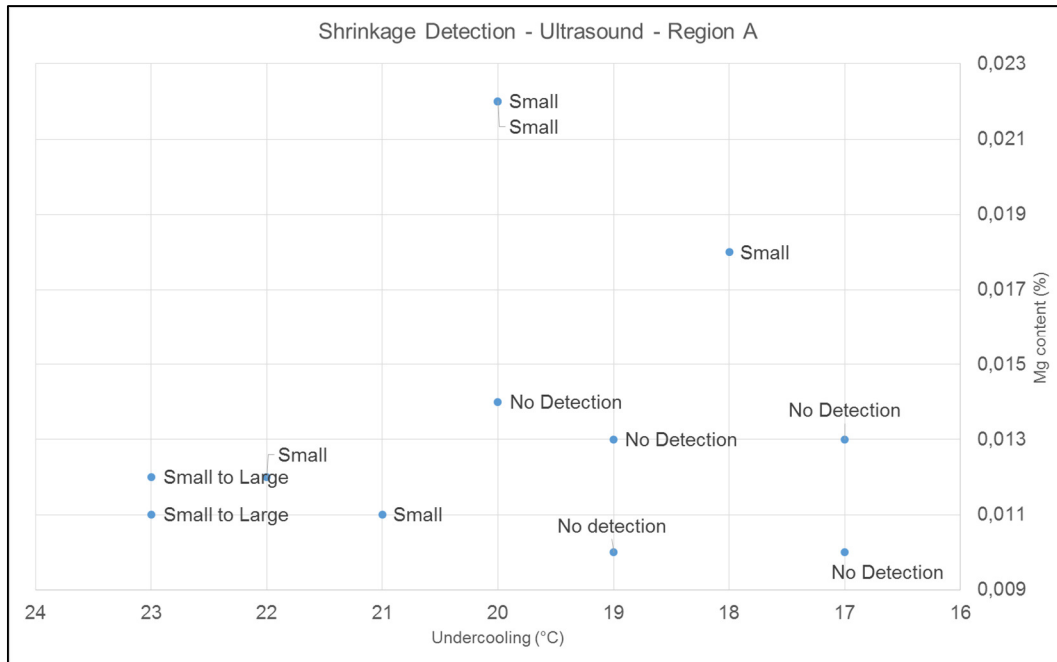
4.4.2 Ultrasonic Testing

Although X-ray already detected some of the porosities that occurred in the samples, figure 54, the ultrasonic testing identifies samples with smaller porosities than the X-Ray resolution is capable of identifying, but due to the specimen geometry and region of shrinkage occurrence, only region A was investigated using this technique. Figure 58 shows the results of the test for region A, characterizing the size of porosity into the same sizes identified by X-ray analysis, small, medium and large.

It is possible to observe a certain trend among the samples, where the larger porosities occurred in samples with 22 to 23 °C of undercooling and 0.011 to 0.012% of magnesium. Small defects occurred in samples with 20 to 21 °C of undercooling for

0.011% of magnesium and for 0.023% of magnesium and in the samples with 18 °C of undercooling and 0.018% of magnesium.

Figure 58: Diagram showing the ultrasonic testing results for each experimental condition - Region A.



Source: Author 2018

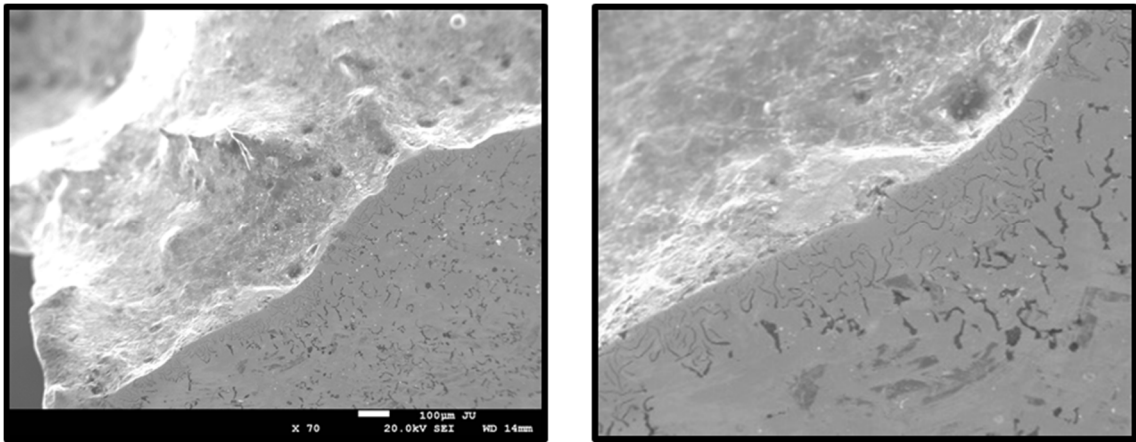
The samples from the remaining test conditions did not have any porosity detected by ultrasound analysis.

4.4.3 Pore Surface Analysis with SEM and EDS

In order to understand the difference between the types of porosities identified by ultrasound and x-ray the samples were analysed using SEM-EDS.

Figure 59 shows one of the types of porosity that were found, this type of porosity did not present any crystalline graphite layer on its surface, and the EDS analysis indicates the presence of oxygen in the surface, evidenced also by the presence of a lamellar graphite rim. According to literature, these characteristics are indicative that this type of defect was formed at a high temperature and in contact with the oxygen in the atmosphere. [41] This type of porosity represents the larger porosity found in the samples using x-ray and ultrasound.

Figure 59: Large size porosity. The figure to the right highlights the lamellar graphite rim in the porosity surface.

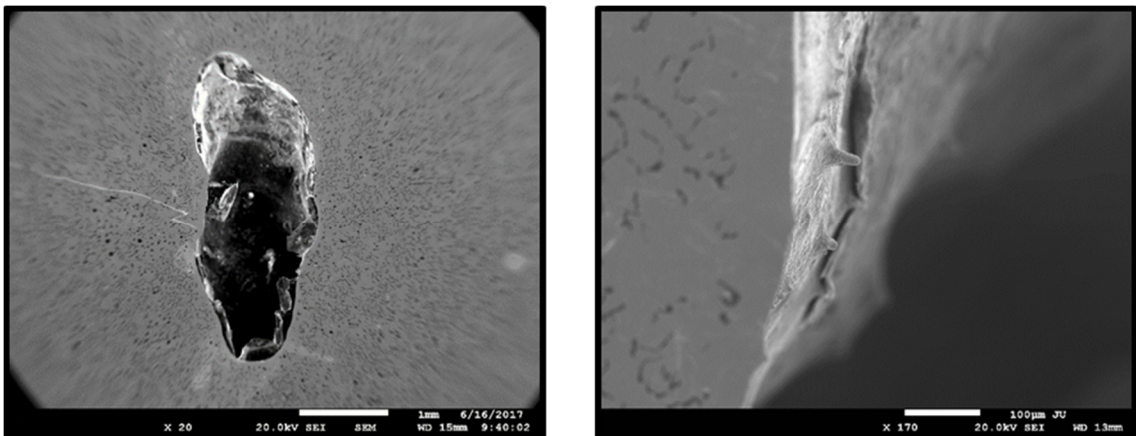


Source: Author 2018

A mass flow from the region of the porosity to another region during the solidification shrinkage may have formed the porosity.

Figure 60 shows the porosity classified as medium size. Unlike the previous type of porosity, this one presents a crystalline graphite layer inside the defect and no sign of oxidation, indicating that the porosity formed without contact to the atmosphere. The dendrites observed inside the porosity are very similar to the ones found inside the previous defect, which indicates that they probably formed at the same temperature level; a mass flow inside the specimen may also have caused this type of defect.

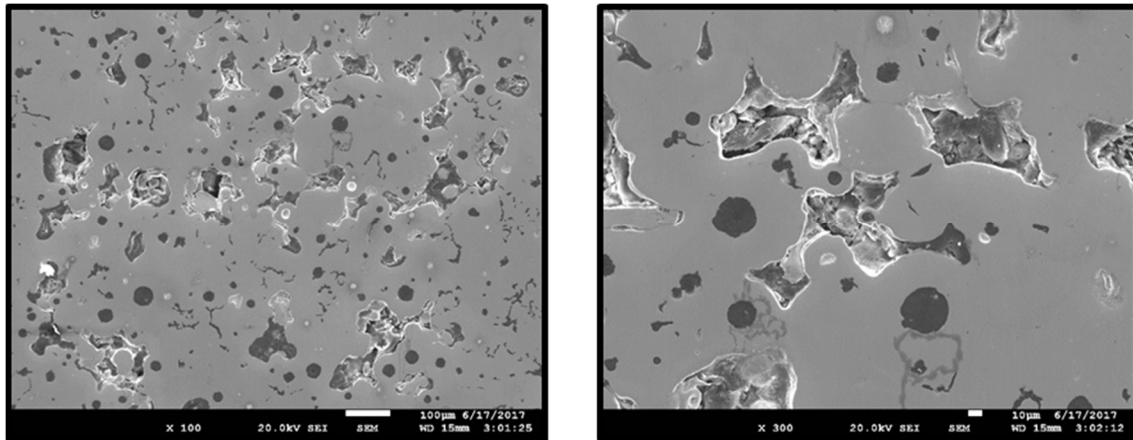
Figure 60: Medium size porosities.



Source: Author 2018

Figure 61 shows the small type of porosity identified in the samples; this type of porosity is smaller when compared to the other two types and is formed in the last to freeze regions between the eutectic cells.

Figure 61: Small size porosities, formed in the last to freeze areas.



Source: Author 2018

4.4.4 Porosity Formation Related to the Parameters under Study

The characterization using SEM and EDS showed that there are different types of defects generated in different experimental conditions. Medium to large porosities in the samples with large undercooling and 0.010% of magnesium, which seems to have formed in the beginning of the solidification, and small, end of solidification shrinkage porosities, in the samples with small undercooling and magnesium content above 0.018%.

One possible explanation to the different defects detected in the two extremes of the experiment, large porosities for low inoculation and low magnesium and small porosities for medium to high inoculation and high magnesium lies in how the microstructure formation in region B is influenced by these distinct experimental conditions.

The white eutectic in the surface combined with little presence of dendrites in the centre of region B section could be facilitating the metal flow needed to form the large defects seen for high undercooling and magnesium content of 0.011%. For medium to low undercooling, the refinement of the structure and larger presence of dendrites in the centre of region B must have made it harder for the metal to flow through this region and the type of defects formed in these samples are smaller and more influenced by other variables.

Regarding nodularity, although the shrinkage porosities found in the samples with higher nodularity were classified as small they are still large enough to be detected

by ultrasound and x-ray inspections while the porosities found in other samples during metallographic inspections were too small to be detected by these types of inspection. This is in accordance with other authors' findings that high nodularity has a strong influence over shrinkage porosity occurrence. A possible explanation for this behaviour is that the increased presence of SGI eutectic would transfer less expansion to the liquid during its formation, since it is enveloped by the austenite shell sooner than the CGI eutectic, resulting in more shrinkage from the liquid metal in last to freeze areas.

The increase in homogeneity of the CGI eutectic structure in zone 2, observed by the use of colour etching, and the reduction, or absence, of porosity in the samples with small undercooling and magnesium below 0.018% suggests that an increase in inoculation may be beneficial for shrinkage porosity control, provided that magnesium content is kept in a maximum level. This level may be between 0.014 and 0.018%, where there is a gap in experimental results from the present study.

There is another important observation regarding the refinement that low undercooling seems to generate in the CGI eutectic structure. This refinement might be promoting a reduction in segregation, since the CGI eutectic cells grows more evenly through the section, and transferring more expansion into the liquid, since CGI eutectic cells keep their contact with the liquid for a longer period during solidification. Therefore, reducing the probability for internal shrinkage defects occurrence.

The CGI eutectic cell mean diameter and area fraction measurements did not show any correlation with magnesium content and inoculation level, this could have been influenced by errors during the measurements generated by two different sources related to the boundary between eutectic cells and last to freeze areas. The first source would be the accuracy of the colour etching to reveal the exact boundary between the eutectic cell and the last to freeze area, and the second is the difficulty to determine this same boundary manually during image treatment to perform the measurements.

The eutectic cells measured by this study are significantly smaller than the eutectic cells measured in other, similar studies. The eutectic cell area fraction measured during the study falls into the size suggested by other author as an eutectic area fraction to which there is more shrinkage porosity detection. [3] Further studies are required to understand why this difference in eutectic cell size exists.

5 CONCLUSIONS

Specimen susceptibility to shrinkage porosity occurrence

The specimen developed during the study has shown different levels of porosity related to the variation in the parameters under study, with larger defects occurring for high undercooling and magnesium contents around 0.010% and smaller defects occurring in samples with low undercooling and magnesium contents above 0.018%.

Characterization of porosities

Porosity characterization revealed three types of porosities in the samples under study, a large porosity, with no carbon layer covering its surface, a medium porosity, with a carbon layer covering its surface and small shrinkage porosities found in last to freeze areas, between eutectic cells. The first two probably formed during early stages of solidification and the third formed close to the end of the solidification.

Influence of magnesium content and undercooling over microstructure and its effect over porosity formation

The increase in magnesium content and inoculation level provoked an increase in nodularity in regions A and C of the samples, especially for magnesium levels above 0.018%. The samples with higher nodularity presented larger porosities in last to freeze areas. Samples of nodularity close to 20% but magnesium below 0.013% did not show this same behaviour, presenting only very small shrinkage porosities in last to freeze areas.

Eutectic cell structure in the samples became more homogeneous with an increase in inoculation level below magnesium content of 0.018%, with the last to freeze area more evenly distributed between the eutectic cells.

A relation between the results of eutectic cell area fraction and mean diameter measurements and the porosity occurrence has not become clear during the study. There are two possible sources of error that could influence these results, the accuracy

of the colour etching to determine the boundary between eutectic cell and last to freeze areas and the difficulties to determine this same boundary manually during treatment of the images.

The different set of parameters had influence on how the microstructure in Region B of the sample formed, with direct chill and a coarser structure in samples with large undercooling and no direct chill and a finer structure in samples with small undercooling. The difference observed in this region might be the reason why there are different types of shrinkage in these two conditions.

6 FUTURE WORK

The EPMA method for elemental mapping shall be employed to understand the chronology of solidification, especially in the regions close to shrinkage for medium to large types of porosities to the small end of solidification shrinkage porosity found in this study.

Influence of Carbon Equivalent over porosity formation should also be studied, by repeating this experiment with increasing CE, from hypoeutectic compositions to hypereutectic compositions.

Cooling rate effect should also be studied by using different moulding materials and coating to cast the same specimen.

7 BIBLIOGRAPHIC REFERENCES

- [1] GUESSER, W. L., GUEDES, L.C., The new generation engines and the challenges for the foundry industry. AEA - SIMEA 2016, São Paulo.
- [2] DAWSON, S., INDRA, F., Compacted graphite iron – A new material for highly stressed cylinder blocks and cylinder heads. 28th International Vienna Motor Symposium on 27 April 2007
- [3] VAZEHRAD, S., ELFSBERG, J., DIOSZEGI, A., Study of microstructure and silicon segregation in cast iron using color etching and electron microprobe analysis. Mater. Charact. 104, 132–138 (2015)
- [4] ASM Metals Handbook Volume 15 Casting 2008
- [5] ELLIOTT, Roy. Cast Iron Technology. 1st Edition, Butterworth & Co., 1988
- [6] SCHELLENG R.D., Cast Iron (With Vermicular Graphite), U.S. Patent 3,421,886, May 1965
- [7] DAWSON, S., “Process Control for the Production of Compacted Graphite Iron”, AFS Casting Congress Kansas City, 4-7 May, (2002)
- [8] DAWSON, S., GUESSER, W. L., Castability, Product Design, and Production of Compacted Graphite Irons, ASM Handbook, Volume 1A, Cast Iron Science and Technology, 2017, pp 665 - 675.
- [9] DAWSON, S., HOLLINGER I., ROBBINS, M., DAETH, J., REUTER, U., and SCHMIDT, H. “The Effect of Metallurgical Variables on the Machinability of Compacted Graphite Iron”, *Presented at SAE International Congress*, Detroit, (March 2001)
- [10] ROSA, S. N., DINIZ, A. E., VENTURA, C. E. H., GUESSER, W. L., ANDRADE, C. L. F., Effects of the Titanium content variation in the longitudinal turning of compacted graphite iron. 20th International Congress of Mechanical Engineering, Gramado, Brazil, 2009.

[11] GUESSER, W., DAWSON, S. e SCHROEDER, T. Production Experience With Compacted Graphite Iron Automotive Components. *AFS Transactions*. 2001, Vols. 01-071.

[12] PIESKE, A; CHAVES Filho, L M; ASSADA, F. Obtenção de ferros fundidos com grafita vermicular. Congresso ILAFA, nov/76, Rio de Janeiro. Publicado em *Fundicion*, nº 211, março 1978.

[13] KURZ M. and FISHER, D.J., 'Fundamentals of Solidification', 3rd ed., Trans Tech Publications Ltd, Uetikon-Zuerich, Switzerland, 1992

[14] DIÓSZEGI, A., LIU, K.Z., SVENSSON, I.L.: Inoculation of Primary Austenite in Grey Cast Iron. *International Journal of Cast Metals Research*. Vol. 20, no. 2, pp. 68-72., 2007.

[15] CHAO, L., DU, W.-C, 'Macro-micro modeling of solidification' Proceedings of the National Science Council, Part A: Physical Science and Engineering (China), vol. 23, no. 5, pp. 622-629, 1999.

[16] HERNANDO, J., GHASSEMALI, E., DIÓSZEGI, A. The morphological evolution of primary austenite during isothermal coarsening *Materials Characterization*, 131, 492-499. 2017.

[17] HOLMGREN, D., KÄLLBOM, R., SVENSSON, I.L., ' Influences of the graphite growth direction on the thermal conductivity of cast iron' *Metall. Mater. Trans. A*, 38, pp. 268-75, 2007.

[18] MINKOFF: *The Physical Metallurgy of Cast iron*, John Wiley & Son, 1983, ISBN: 0471-90006-0.

[19] LOPER, C. R., Jr. Inoculation of Cast Iron – Summary of current Understanding, *AFS Transactions*, 1999, 36, pp. 523-28.

[20] RIVERA, G., CALVILLO, P.R., BOERI, R., HOUBAERT, Y., SIKORA, J., Examination of the solidification macrostructure of spheroidal and flake graphite cast irons using DAAS and EBSD. *Materials Characterization*. Volume 59, Issue 9, 2008.

- [21] BOERI, R. E. The solidification of Ductile Cast Iron, PhD Thesis. 1989 The University of British Columbia.
- [22] BOERI, R. E. and SIKORA, J., Solidification macrostructure of spheroidal graphite cast iron *Int. J. Cast Met. Res.*, 2001, 13, pp. 307-13.
- [23] ITOFUJI, H., KAWANO, Y., INOYAMA, N., 'The formation mechanism of compacted-vermicular graphite in cast irons' *AFS Trans.*, 91, pp. 831-40 1983.
- [24] STEFANESCU, D. M., MARTINEZ, F., CHEN, I. G., 'Solidification behavior of hypoeutectic and eutectic compacted graphite cast irons - Chilling tendency and eutectic cells' *AFS Trans.*, 91, pp. 205-16, 1983.
- [25] L. Bäckerud, K. Nilsson and H. Steen, in *The Metallurgy of Cast Iron*, B. Lux, I. Minkoff and F. Mollard, Eds., Georgi Publishing, Switzerland (1975) 625.
- [26] STEFANESCU, 'Thermal analysis – Theory and applications in metal castings.' *International Journal of Metal Casting.*, vol. 9, Issue 1, 2015.
- [27] KONIG, M., SVENSSON, I. L., WESSÉN, M., "The Influence of Alloying elements on Chill Formation in CGI", *Proceedings of Science and Processing of Cast Iron - 9*, November 9-13, 2010, Luxor, Egypt, pp.126-31.
- [28] KONIG, M., "Microstructure Formation during Solidification and Solid State Transformation in Compacted Graphite Iron", PhD Thesis, Chalmers University of Technology, Gothenburg, Sweden, (2011)
- [29] WETTERFALL, S.-E, FRIEDRIKSSON, H. AND HILLERT, M. Solidification of nodular cast iron. *Journal of the Iron and Steel Institute*, 1972. 210(5): p. 323-333.
- [30] RIVERA, G. L., BOERI, R. E., SIKORA, J. A. Revealing the solidification structure of nodular iron. *Cast Metals*, Volume 8, number 1, pp 1- 5. 1995
- [31] VAZEHRAD, S., ELFSBERG, J., DIOSZEGLI, A., On Factors Influencing Macro Shrinkage Porosity Formation in Compacted Graphite Iron, *Materials Science Forum*. 790-791. 429-434. 10.4028/www.scientific.net/MSF.790-791.429. 2014

- [32] VAZEHRAD, S *Shrinkage porosity characterization in compacted cast iron components*, Master Thesis, KTH Royal Institute of Technology, Stockholm, 2011
- [33] CAMPBELL, J., "Castings", Oxford, Butterworth-Heinemann Ltd, 2nd Edition, 2003.
- [34] STEFANESCU, D. M., "Computer Simulation of Shrinkage Related Defects in Metal Casting- A Review," *International Journal of Cast Metals Research*, Vol. 18, No. 3, pp. 129-143, 2005.
- [35] MEREDITH, J.F., "Defect Diagnosis in Ferrous Castings", *Metal Casting Technologies*, Vol.46, no.5, pp.26-27, (2000)
- [36] FREDRIKSSON, H., ÅKERLIND, U., "Materials Processing During Casting", ISBN: 0-470-01514-4, (2006)
- [37] CHEN, J.Y., WU, D. H., LIU, P. C., and LOPER, C. R., 'Liquid Metal Channel Formation in Compacted/Vermicular Graphite Cast Iron Solidification' *AFS Trans.*, 94, pp. 537-544, (1986)
- [38] TENAGLIA, N., BOERI, R., RIVERA, G., MASSONE, J., 'Study of Shrinkage Porosity in Spheroidal Graphite Cast Iron' 10th International Symposium on the Science and Processing of Cast Iron, Mar del Plata, Argentina 2014.
- [39] RIVERA G. L., BOERI R., and SIKORA, J.. "Revealing and characterizing solidification structure of ductile cast iron." *Materials science and technology* 18.6, pp. 691-697, 2002.
- [40] PEHLKE, R.D., 'Formation of porosity during solidification of cast metals' *Foundry Process: Their chemistry and Physics*; Warren, Michigan, USA, pp. 427-445 1988.
- [41] ELMQUIST, L., DIOSZEGI, A., ADOLFSSON, S., *Characterizing Shrinkage Porosity in Gray Cast Iron Using Microstructure Investigation*. AFS Transactions, Schaumburg, IL USA 2008.
- [42] SKALAND, T., *A new approach to ductile iron inoculation*. AFS Transactions, 01-078 USA 2001.

[43] SEARGENT, G F & EVANS, E R. The production and properties of compacted graphite irons. *The British Foundryman*, vol 71, nº 5, p. 115-124, 1978.

[45] MOTZ, J. M.: Microsegregation- an Easily Unnoticed Influencing Variable in the Structural Description of Cast Materials, *Praktische Metallographie*, Vol 25, No 6, June 1988, p 285-293, (1988).

[46] DOMEIJ, B., HERNANDO, J.C. & DIÓSZEGI, A. *Metall and Materi Trans B* (2018) 49: 2487. <https://doi.org/10.1007/s11663-018-1274-z>